Journal of the Mechanics and Physics of Solids 59 (2011) 216–236

Contents lists available at ScienceDirect

Journal of the Mechanics and Physics of Solids

journal homepage: www.elsevier.com/locate/jmps

Reversible stress-induced martensitic phase transformations in a bi-atomic crystal

Ryan S. Elliott [a,*], Nicolas Triantafyllidis [b,c,d], John A. Shaw [c]

[a] Department of Aerospace Engineering and Mechanics, University of Minnesota, Minneapolis, MN 55455, USA
[b] Laboratoire de Mécanique des Solides & Departement de Mécanique, Ecole Polytechnique, Palaiseau 91128, France
[c] Department of Aerospace Engineering, University of Michigan, Ann Arbor, MI 48109, USA
[d] Department of Mechanical Engineering, University of Michigan, Ann Arbor, MI 48109, USA

ARTICLE INFO

Article history:
Received 4 June 2010
Received in revised form
27 October 2010
Accepted 30 October 2010
Available online 5 November 2010

Keywords:
Phase transformation
Finite strain
Stability and bifurcation
Buckling
Thermoelastic material

ABSTRACT

In an earlier work, Elliott et al. [2006a, Stability of crystalline solids—II: application to temperature-induced martensitic phase transformations in bi-atomic crystals. Journal of the Mechanics and Physics of Solids 54(1), 193–232], the authors used temperature-dependent atomic potentials and path-following bifurcation techniques to solve the nonlinear equilibrium equations and find the temperature-induced martensitic phase transformations in stress-free, perfect, equi-atomic binary B2 crystals. Using the same theoretical framework, the current work adds the influence of stress to study the model's stress-induced martensitic phase transformations.

The imposition of a uniaxial Biot stress on the austenite (B2) crystal, lowers the symmetry of the problem, compared to the stress-free case, and leads to a large number of stable equilibrium paths. To determine which ones are possible reversible martensitic transformations, we use the (kinematic) concept of the *maximal Ericksen–Pitteri neighborhood* (max EPN) to select those equilibrium paths with lattice deformations that are closest, with respect to lattice-invariant shear, to the austenite phase and thus capable of a reversible transformation. It turns out that for our chosen parameters only one stable structure (distorted αIrV) is found within the max EPN of the austenite in an appropriate stress window. The energy density of the corresponding configurations shows features of a stress-induced phase transformation between the higher symmetry austenite and lower symmetry martensite paths and suggests the existence of hysteretic stress–strain loops under isothermal load–unload conditions. Although the perfect crystal model developed in this work over-predicts many key material properties, such as the transformation stress and the Clausious–Clapeyron slope, when compared to real experimental values (based on actual polycrystalline specimens with defects), it is—to the authors' knowledge—the first atomistic model that has been demonstrated to capture all essential trends and behavior observed in shape memory alloys.

1. Introduction

An interesting property of many crystalline materials is their ability to undergo solid-to-solid phase transformations when subjected to changes in temperature or applied load. Of interest here are *diffusionless* PTs, also termed *martensitic* or *displacive* transformations. These involve the material's transformation from a high symmetry crystal structure, *austenite*, to a

* Corresponding author.
E-mail address: elliott@aem.umn.edu (R.S. Elliott).

0022-5096/$ - see front matter © 2010 Elsevier Ltd. All rights reserved.
doi:10.1016/j.jmps.2010.10.011

lower symmetry structure, *martensite*, by a coordinated motion of the crystal's atoms in response to an instability. In such a transformation, neighboring atoms move small relative distances compared to their lattice spacing by a process that involves latent heat (a *first-order* PT). Of particular importance are *proper* MTs which exhibit a group–subgroup relation between the austenite and martensite phases, and are thus, likely to be reversible MTs.

An important technological application of these proper martensitic phase transformations involves shape memory alloys (SMAs) which exhibit two remarkable properties: the shape memory effect and pseudoelastic behavior. The first refers to the capability of the polycrystalline alloy to erase relatively large (up to 8%) mechanically induced strains by moderate temperature increases. The second pertains to the ability of the alloy to accommodate strains of this magnitude and recover upon unloading via a hysteretic stress–strain loop. Of the long list of alloys that exhibit these remarkable properties, NiTi-based alloys have the best memory and structural properties as polycrystals, and as a result, are the most popular and commercially viable (an excellent presentation of this subject can be found in Bhattacharya, 2003). It is for this reason that the present work takes an ordered equi-atomic binary alloy as our prototype for a shape memory alloy.

There is a voluminous literature on SMA modeling at different scales, the review of which is beyond the scope of this work. Of interest here are atomistic models for perfect SMA alloy crystals, which can simulate temperature- and stress-induced martensitic phase transformations. One can distinguish three different approaches in the atomistic modeling of SMAs:

First, at the most fundamental level, are the quantum mechanics based first-principles density function theory (DFT) methods. These methods are valuable for investigating the energy differences between many phases of a material and for studying the stability of these phases at 0 K (see Huang et al., 2002, 2003b; Parlinski and Parlinska-Wojtan, 2002; Parlinski et al., 2003; Ye et al., 1997). This approach allows one to calculate atomic-level information regarding energies, forces, and stresses independent of any empirical atomic potential fitting. DFT calculations, such as those of Huang et al. (2002, 2003b), performed at 0 K show that the B2 cubic austenite crystal structure of NiTi is unstable since NiTi has imaginary phonon frequencies at 0 K. This indicates that temperature effects are responsible for the existence of a stable austenite phase in NiTi at higher temperatures (Elliott and Karls, submitted). However, direct DFT-based studies of temperature effects on the behavior of PTs in NiTi and other SMAs are extremely computationally intensive.

The second atomistic approach is based on molecular dynamics (MD) or Monté Carlo (MC) simulations and is capable of capturing temperature effects which are necessary for studying PTs. In particular, MD simulations based on different phenomenological atomic interaction potentials have been useful for exploring the dependence of PTs on properties such as temperature, composition, concentration of defects, etc. (see Entel et al., 1999, 2000; Grujicic and Dang, 1995; Ishida and Hiwatari, 2007; Meyer and Entel, 1998; Ozgen and Adiguzel, 2003; Rubini and Ballone, 1995; Shao et al., 1996; Wang et al., 2006). However, MD and MC simulations do not provide a systematic approach for identifying all equilibrium phases of the system of interest. Instead, they require many time consuming calculations using different initial data. Even when such extensive calculations are performed, there is no way to know how many other possible equilibrium phases of the system have been missed. Furthermore, the extension of MD and MC simulations to larger length- and time-scales in order to study the formation and evolution of microstructures in SMAs is impractical except on the largest of currently available parallel-computing systems. Even on these systems, the size of the simulations of interest would require considerable computation time.

This leads to the third approach, which is a bifurcation-based method, initially proposed by Ericksen (1992), to study phase transformations in SMAs. The bifurcation theory approach has previously been used to study the stability of perfect crystals by Thompson and Shorrock (1975), Milstein et al. (1980) and by Milstein et al. (1995) to investigate reconstructive PTs in metals. More recently, these methods have been used by Elliott et al. (2002, 2006a) to investigate the temperature-dependent transformations in binary equi-atomic B2 crystals at zero stress.

In this work the material's continuum energy density is explicitly derived from a set of phenomenological effective interaction potentials (EIPs), which are interatomic potentials that depend explicitly on temperature (see Guthikonda and Elliott, 2008, 2009, in press). Subsequently, stationary points are identified, with respect to strain and internal atomic displacements, to find all equilibrium solutions in a prescribed temperature range. The stable parts of these paths can then be identified, as explained in Elliott et al. (2006b). This method brings the problem of finding the equilibrium phases of a perfect crystal as a function of temperature into the realm of bifurcation and stability theory, since it requires solving a nonlinear system of equations with a low number of degrees of freedom. In contrast to the MD and MC methods, a bifurcation and stability analysis *systematically* determines both stable and unstable equilibrium configurations, providing additional information about equilibrium paths connecting different phases.

The current work, an extension of Elliott et al. (2006a) and Elliott (2007), adds the influence of stress to study stress-induced transformations. The application of a macroscopic stress to the infinite, perfect bi-atomic crystal is considerably more complicated, due to the substantial increase in number of equilibrium solutions, as compared to the stress-free case.[1] However, once the equilibrium solution set has been obtained and unstable paths eliminated, one needs to determine which of the remaining stable equilibrium paths, still relatively numerous, are potential reversible martensitic transformations. We will use the (kinematic) concept of the *maximal Ericksen–Pitteri neighborhood* to select those equilibrium solutions with lattice deformations *closest* to the austenite phase as the relevant ones.

[1] The large number of equilibrium solutions is a common feature of nonlinear systems with high symmetry, and in this way our investigation is similar to the study of axially compressed cylinders by Wohlever and Healey (1995).

The paper is organized as follows: a brief description of the model is given in Section 2 which presents the Cauchy–Born kinematics, equilibrium path equations, stability criteria for these paths, and the concept of the maximum Ericksen–Pitteri neighborhood. The results are presented next in Section 3, starting with the case of stress-free, temperature-induced transformations, followed by stress-induced transformations at a fixed temperature and uniaxial Biot stress loading (directed along the [1 1 0] direction in the austenite's cubic system). Stress-induced transformations at different temperatures and another loading direction ([1 1 1] in the austenite's cubic system) are considered next, and finally the influence of the loading device is investigated. The work is concluded by a critical discussion of the results in Section 4. Details on the selection of an appropriate unit cell for the numerical calculations are presented in Appendix A.1 and on the selection of temperature-dependent atomic potentials are given in Appendix A.2.

2. Modeling

This section describes the atomistic model for perfect bi-atomic lattices used to investigate the stability of equilibrium configurations subjected to a uniform macroscopic stress field. A brief presentation of the Cauchy–Born kinematic assumption and the derivation of the material's energy density function is followed by a statement of the equilibrium equations. Next the stability criteria (Cauchy–Born and phonon) are presented. The section concludes with a description of the process used to select proper martensitic transformation equilibrium paths from among a large number of stable equilibrium solutions.

2.1. Cauchy–Born kinematics

An M-lattice consists of a set of M inter-penetrating *sub-lattices* each of which is positioned relative to an underlying (imaginary) Bravais lattice (see Fig. 1 for an example of a two-dimensional 4-lattice). The arrangement of atoms about each lattice point is specified by a set of M three-dimensional vectors $\mathbf{P}[\alpha]\ \alpha = 0,1,2,\ldots,M-1$; called the *fractional position vectors*, also depicted in Fig. 1.

Each atom in the crystal is uniquely identified by specifying the sub-lattice index α and lattice point ℓ. The reference position vector of each atom is thus defined by

$$\mathbf{X}\begin{bmatrix}\ell\\ \alpha\end{bmatrix} = \mathbf{X}[\ell]+\mathbf{P}[\alpha],$$

$$\mathbf{X}[\ell] \equiv \ell^i \mathbf{G}_i, \quad \ell^i \in \mathbb{Z},$$

$$\mathbf{P}[\alpha] \equiv P^i[\alpha]\mathbf{G}_i, \quad 0 \le P^i[\alpha] < 1;\ \alpha = 0,\ldots,M-1; \tag{2.1}$$

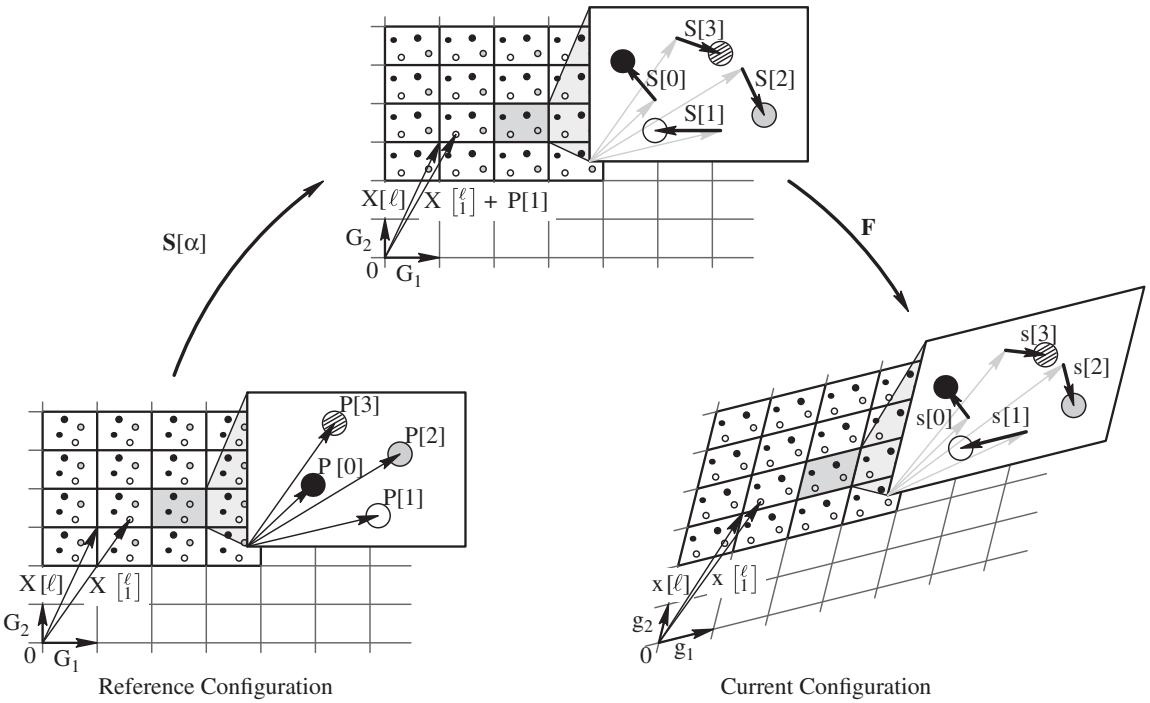

Fig. 1. Cauchy–Born (CB) kinematics description of shifts leading to the current configuration of a two-dimensional, 4-lattice crystal.

where $\mathbf{X}[\ell]$ is the reference position of the underlying Bravais lattice point ℓ, and $\mathbb{Z}$ is the set of all (positive and negative) integers. The label ℓ for the underlying Bravais lattice point is a short-hand notation referring to the triplet of integers $\ell=(\ell^1,\ell^2,\ell^3)$, $\mathbf{P}[\alpha]$ is the fractional position vector for atom α, and $\mathbf{G}_i$ are the reference lattice vectors.[2]

Of interest here are deformations that take an M-lattice into another M-lattice. These deformations can be expressed in terms of the uniform deformation $\mathbf{F}$ of the underlying Bravais lattice vectors and a set of internal shift vectors $\mathbf{S}[\alpha]$ corresponding to translations of the sub-lattices. Cauchy–Born (CB) kinematics are formulated as shown in Fig. 1. In this formulation, the internal shifts $\mathbf{S}[\alpha]$ are first applied to the reference configuration, and then the uniform deformation $\mathbf{F}$ is applied to this intermediate configuration. The current position vector of atom $\left[\begin{smallmatrix}\ell\\ \alpha\end{smallmatrix}\right]$ is

$$\mathbf{x}\begin{bmatrix}\ell\\ \alpha\end{bmatrix}=\mathbf{F}\cdot\left(\mathbf{X}\begin{bmatrix}\ell\\ \alpha\end{bmatrix}+\mathbf{S}[\alpha]\right)=F^i{}_j\left(X^j\begin{bmatrix}\ell\\ \alpha\end{bmatrix}+S^j[\alpha]\right)\mathbf{G}_i=\left(X^j\begin{bmatrix}\ell\\ \alpha\end{bmatrix}+S^j[\alpha]\right)\mathbf{g}_j, \tag{2.2}$$

where $\mathbf{g}_i$ are the current lattice basis vectors defined as $\mathbf{g}_i=\mathbf{F}\cdot\mathbf{G}_i$. Notice that Eq. (2.2) includes all rigid-body motions of the crystal. However, to find equilibrium paths and to determine their stability, a set of kinematics for which rigid-body modes have been eliminated is required. The following additional constraints are added

$$\mathbf{F}\equiv\mathbf{U},\quad \mathbf{S}[0]\equiv\mathbf{0}, \tag{2.3}$$

where $\mathbf{U}=\mathbf{U}^{\mathrm{T}}$ is the symmetric right stretch tensor. Eq. $(2.3)_1$ is equivalent to setting $\mathbf{R}$, the rotation part of the polar decomposition $\mathbf{F}=\mathbf{R}\cdot\mathbf{U}$, to the identity. Eq. $(2.3)_2$ eliminates rigid-body translations of the crystal by restraining one of the sub-lattices against translation.

2.2. Energy density

The general methodology introduced in this paper is applicable to any type of atomic effective interaction potential (EIP) (see Appendix A.2). However, for computational speed, pair potentials are used in this work for the calculations of the stress- and temperature-dependent equilibrium paths. Although there are well-known deficiencies associated with the use of pair potentials, e.g., the Cauchy relations, they capture much of the essential physics required to model martensitic phase transformations in perfect M-lattices, as shown in Elliott et al. (2006a).

Our model constructs the material's internal energy per unit reference volume $\widetilde{W}$ from atomic interaction functions. The temperature-dependent energy function $\psi[\left[\begin{smallmatrix}\ell\\ \alpha\end{smallmatrix}\right]](\theta)$ associated with each atom $\left[\begin{smallmatrix}\ell\\ \alpha\end{smallmatrix}\right]$ in the crystal is

$$\psi\begin{bmatrix}\ell\\ \alpha\end{bmatrix}(\theta)=\frac{1}{2}\sum_{\left[\begin{smallmatrix}\ell'\\ \alpha'\end{smallmatrix}\right]\in\Omega}\phi_{\alpha\alpha'}\left(r\begin{bmatrix}\ell & \ell'\\ \alpha & \alpha'\end{bmatrix};\theta\right), \tag{2.4}$$

where $\phi_{\alpha\alpha'}$ is the interaction pair potential between atoms of type α and α' and the summation runs over all atoms $\left[\begin{smallmatrix}\ell'\\ \alpha'\end{smallmatrix}\right]$ in the crystal Ω. The *self-interaction energy* is assumed to be zero, i.e., $\phi_{\alpha\alpha}(0,\theta)\equiv 0$. The distance between two atoms $\left[\begin{smallmatrix}\ell\\ \alpha\end{smallmatrix}\right]$ and $\left[\begin{smallmatrix}\ell'\\ \alpha'\end{smallmatrix}\right]$ is

$$r\begin{bmatrix}\ell & \ell'\\ \alpha & \alpha'\end{bmatrix}\equiv\left\|\mathbf{x}\begin{bmatrix}\ell'\\ \alpha'\end{bmatrix}-\mathbf{x}\begin{bmatrix}\ell\\ \alpha\end{bmatrix}\right\|, \tag{2.5}$$

where $\|\cdot\|$ is the Euclidean norm. The internal potential energy density per unit reference volume for the crystal is calculated for a representative unit cell, $\ell=0$, to be

$$\widetilde{W}(\mathbf{U},\mathbf{S};\theta)=\frac{1}{V}\sum_{\alpha=0}^{M-1}\psi\begin{bmatrix}0\\ \alpha\end{bmatrix}(\theta)=\frac{1}{2V}\sum_{\alpha=0}^{M-1}\sum_{\left[\begin{smallmatrix}\ell'\\ \alpha'\end{smallmatrix}\right]\in\Omega}\phi_{\alpha\alpha'}\left(r\begin{bmatrix}0 & \ell'\\ \alpha & \alpha'\end{bmatrix};\theta\right), \tag{2.6}$$

where $\mathbf{S}\equiv(\mathbf{S}[1],\mathbf{S}[2],\ldots,\mathbf{S}[M-1])$ and $V=\mathbf{G}_1\cdot(\mathbf{G}_2\times\mathbf{G}_3)$ is the reference volume of one M-lattice unit cell.

To completely determine the energy density, one must consider the potential energy of the loading device. Different types of loading devices are possible. In this case, the most straightforward loading is to impose the *Biot stress*, denoted by $\boldsymbol{\Pi}_{\mathrm{B}}$, which is the work-conjugate of the strain measure $\mathbf{U}-\mathbf{I}$. We take the Biot stress to be of the form $\boldsymbol{\Pi}_{\mathrm{B}}=\Sigma\mathbf{N}\mathbf{N}$, where Σ is the magnitude of the uniaxial-like stress along reference direction $\mathbf{N}$. The corresponding potential energy per unit reference volume is written as[3]

$$\widetilde{\mathcal{E}}(\mathbf{U},\mathbf{S};\theta,\Sigma)=\widetilde{W}(\mathbf{U},\mathbf{S};\theta)-\boldsymbol{\Pi}_{\mathrm{B}}:(\mathbf{U}-\mathbf{I})=\widetilde{W}(\mathbf{U},\mathbf{S};\theta)-\Sigma(\mathbf{N}\cdot\mathbf{U}\cdot\mathbf{N}-1). \tag{2.7}$$

We recognize that the Biot stress measure $\boldsymbol{\Pi}_{\mathrm{B}}=\Sigma\mathbf{N}\mathbf{N}$ is not actually consistent with the usual notion of uniaxial loading, but it is computationally convenient to reduce the number of degrees of freedom. A more conventional uniaxial loading, prescribed by a similar form of the First Piola–Kirchhoff stress, will be discussed in detail in Section 3.5, but it turns out to give very similar results.

[2] Unless otherwise specified, Latin indices represent spatial tensor components and Einstein's summation convention is employed.

[3] Here the coordinate-free notation $\mathbf{A}:\mathbf{B}$ is given by $A_{ijkl}B_{kl}$ in Cartesian tensor indicial notation.

2.3. Equilibrium paths

Equilibrium solutions are obtained by finding stationary points of the above potential energy $\widetilde{\mathcal{E}}$ with respect to the macroscopic stretch tensor $\mathbf{U}$ and internal shifts $\mathbf{S}[\alpha]$, i.e.,

$$\frac{\partial \widetilde{\mathcal{E}}}{\partial \mathbf{U}} = \mathbf{0}, \quad \frac{\partial \widetilde{\mathcal{E}}}{\partial \mathbf{S}[\alpha]} = \mathbf{0}, \ \alpha = 1,2,\ldots,M-1. \tag{2.8}$$

Eq. $(2.8)_1$ is the statement of *macroscopic* equilibrium with respect to the six independent components of $\mathbf{U}$. Eq. $(2.8)_2$ is the statement of inter-sub-lattice equilibrium with respect to the $3M-3$ components of the internal shift vectors $\mathbf{S}[\alpha]$, $\alpha = 1,2,\ldots,M-1$. It should be noticed at this point that the multilattice description with its internal shifts ensures that the total force applied to every atom in the crystal (by all other atoms) is zero whenever Eqs. (2.8) are satisfied, regardless of the particular atomic potential being considered. A proof of this assertion can be found in Elliott et al. (2006b).

In the results section we show equilibrium paths obtained by either varying the temperature θ (for fixed load Σ) or by varying the load Σ (for fixed temperature θ). Ideally one would like to find all equilibrium paths within a given range of temperatures $\theta \in [\theta_1,\theta_2]$ and stresses $\Sigma \in [\Sigma_1,\Sigma_2]$. This goal can, in principal, be achieved with numerical techniques such as *piecewise-linear continuation methods* (Allgower and Georg, 2003). However, these approaches require a triangulation of the system's configuration space which usually makes the corresponding computations prohibitively expensive. Our approach is to use the theory of path continuation and bifurcation to follow all equilibrium paths that are connected to the reference austenite configuration. All computations for this work were performed with the BFBSYMPAC (Elliott, 2010) software package, which is written in C++.

Starting with the stress-free ($\Sigma = 0$) austenite reference equilibrium configuration at the normalized reference temperature ($\theta = 1$, $\mathbf{U}=\mathbf{I}$, $\mathbf{S}=\mathbf{0}$) and using a numerical continuation method, one follows the *principal equilibrium path* for either constant uniaxial stress or constant temperature. A Keller- or Riks-type arc-length method (Riks, 1979; Allgower and Georg, 2003) is used to find points along the principal equilibrium branch. This facilitates traversing the path across limit-loads that may be encountered (see Elliott et al., 2002; Jusuf, 2010, for further details). Moreover, all singular points are identified on the principal branch and then classified as bifurcation points or limit loads.

Next *secondary equilibrium paths* emerging from each bifurcation point on the principal branch are considered. Each secondary path is identified by an asymptotic analysis about the corresponding bifurcation point (Triantafyllidis and Peek, 1992; Elliott et al., 2002, 2006a). The associated crystal structure is determined and a minimal set of DOFs is identified to describe this equilibrium path (Healey, 1988). In general there are m DOFs ($m \leq 3M+3$), and the corresponding subset of nonlinear algebraic equations (2.8) is solved. For example, here $m=1$ for the principal branch associated with thermal loading.

The singular points on each secondary path are determined next and the corresponding bifurcation points are identified. The emerging bifurcated equilibrium paths are termed *tertiary equilibrium paths* and are constructed in the same way as the secondary paths. The process is repeated in this recursive way, following all the emerging tertiary paths, where our path-following continuation algorithm is stopped due to the large number of paths already obtained.

A comment is in order on avoiding infinitely following closed loop paths. At the beginning of each new path (typically at each new bifurcation point) the displacement DOF vector $\mathbf{u}^\star$ is recorded. The distance of the current equilibrium point $\mathbf{u}(\Sigma)$ on the path at load Σ is monitored and when it again approaches $\mathbf{u}^\star$, within a tolerance parameter ε, i.e., when

$$\|\mathbf{u}^\star - \mathbf{u}(\Sigma)\| \leq \varepsilon, \tag{2.9}$$

the calculations for that equilibrium branch are terminated.

2.4. Stability criteria

The two stability criteria, to be used in this work, for crystalline solids that were proposed in Elliott et al. (2006b) are briefly outlined below for completeness.

(I) *Cauchy–Born (CB) stability*: CB-stability indicates stability with respect to all *quasi-uniform* perturbations, in which both the uniform right stretch tensor $\mathbf{U}$ and the internal shift vectors $\mathbf{S}[\alpha]$ are allowed to vary independently. The crystal is considered CB-stable if $\widetilde{\mathcal{E}}(\mathbf{U},\mathbf{S};\theta,\Sigma)$ is a local minimum, or

$$[\delta\mathbf{U},\delta\mathbf{S}] \begin{bmatrix} \dfrac{\partial^2 \widetilde{\mathcal{E}}}{\partial \mathbf{U}\partial \mathbf{U}} & \dfrac{\partial^2 \widetilde{\mathcal{E}}}{\partial \mathbf{U}\partial \mathbf{S}} \\ \dfrac{\partial^2 \widetilde{\mathcal{E}}}{\partial \mathbf{S}\partial \mathbf{U}} & \dfrac{\partial^2 \widetilde{\mathcal{E}}}{\partial \mathbf{S}\partial \mathbf{S}} \end{bmatrix} \begin{bmatrix} \delta\mathbf{U} \\ \delta\mathbf{S} \end{bmatrix} > 0, \quad \forall [\delta\mathbf{U},\delta\mathbf{S}]^{\mathrm{T}} \neq \mathbf{0}. \tag{2.10}$$

In the above equation the stability operator is symmetric and of dimension $(3M+3)\times(3M+3)$.

(II) *Phonon stability*: The phonon stability criterion indicates stability of an equilibrium path with respect to *bounded perturbations of all wavelengths*. All atoms in the crystal are given their three translational degrees of freedom $u^j[\ell_\chi]$ and the

linearized equations of motion are considered. The corresponding perturbation equations are given by

$$m_\alpha \delta\ddot{u}^j\begin{bmatrix}\ell\\ \alpha\end{bmatrix} = -\sum_{\left[\substack{\ell\\ \alpha}\right]\in\Omega} G^{jk}\overset{o}{\Phi}_{kp}\begin{bmatrix}\ell & \ell'\\ \alpha & \alpha'\end{bmatrix}\delta u^p\begin{bmatrix}\ell'\\ \alpha'\end{bmatrix},$$

$$\overset{o}{\Phi}_{ij}\begin{bmatrix}\ell & \ell'\\ \alpha & \alpha'\end{bmatrix} \equiv \frac{\partial^2\left(\sum_{\left[\substack{\ell''\\ \alpha''}\right]\in\Omega}\psi\left[\substack{\ell''\\ \alpha''}\right]\right)}{\partial u^i\left[\substack{\ell\\ \alpha}\right]\partial u^j\left[\substack{\ell\\ \alpha}\right]}, \tag{2.11}$$

where $\ddot{(\,)} \equiv \partial^2(\,)/\partial t^2$ (t is time), m_α is the mass of atom α, $G^{jk} = \mathbf{G}^i \cdot \mathbf{G}^j$ (with the reference reciprocal lattice vectors defined by $\mathbf{G}^i \cdot \mathbf{G}_j = \delta^i{}_j$) are the components of the metric tensor, and $\overset{o}{\Phi}_{ij}\left[\begin{smallmatrix}\ell & \ell'\\ \alpha & \alpha'\end{smallmatrix}\right]$ are the corresponding stiffness coefficients. Of interest are the normal modes of vibration (eigen-modes of Eq. (2.11)) that are characteristic of the bulk material, meaning the effect of free surfaces on the stability of the crystal is neglected.

Taking advantage of the translational symmetry of the multilattice the corresponding stiffness matrix is block-diagonalized by a block-Fourier transform resulting in the *dynamical matrix* $\mathbb{K}^j{}_k\left[\begin{smallmatrix}\mathbf{k}\\ \alpha\ \alpha'\end{smallmatrix}\right]$, a $3M \times 3M$ matrix (where M is the number of atoms in the unit cell) for each wave vector $\mathbf{k}$, given by

$$\mathbb{K}^j{}_k\begin{bmatrix}\mathbf{k}\\ \alpha\ \alpha'\end{bmatrix} = (m_\alpha m_{\alpha'})^{-1/2}\sum_{\ell'\in\mathbb{Z}^3} G^{jp}\overset{o}{\Phi}_{pk}\begin{bmatrix}0 & \ell'\\ \alpha & \alpha'\end{bmatrix}\exp\left\{-i\mathbf{k}\cdot\left(\mathbf{X}\begin{bmatrix}\ell'\\ \alpha'\end{bmatrix}-\mathbf{X}\begin{bmatrix}0\\ \alpha\end{bmatrix}\right)\right\}, \tag{2.12}$$

where $\mathbb{Z}^3$ is the set of all lattice points in the infinite crystal. The wave vector $\mathbf{k}$ has units of inverse length and ranges over values in the unit cell of the reciprocal reference lattice (multiplied by a factor of 2π)

$$\mathbf{k} \in \{k_i\mathbf{G}^i | -\pi \le k_i < \pi\}. \tag{2.13}$$

The eigenvalues of the dynamical matrix are real (due to the Hermitian nature of $\mathbb{K}$) and satisfy the relation

$$(\omega^{(q)}(\mathbf{k}))^2\Delta\hat{v}^j\begin{bmatrix}\mathbf{k}\\ \alpha\end{bmatrix}^{(q)} = \sum_{\alpha'=0}^{M-1}\mathbb{K}^j{}_p\begin{bmatrix}\mathbf{k}\\ \alpha\ \alpha'\end{bmatrix}\Delta\hat{v}^p\begin{bmatrix}\mathbf{k}\\ \alpha'\end{bmatrix}^{(q)}. \tag{2.14}$$

The squared phonon frequencies $(\omega^{(q)}(\mathbf{k}))^2$ must all be positive for the crystal to be stable,[4] i.e.,

$$(\omega^{(q)}(\mathbf{k}))^2 > 0\begin{cases}\text{for } \mathbf{k}\neq\mathbf{0}, & q = 1,2,\ldots,3M,\\ \text{for } \mathbf{k}=\mathbf{0}, & q = 4,5,\ldots,3M.\end{cases} \tag{2.15}$$

For *material stability* under soft-device loading conditions, as defined in Elliott et al. (2006b), the CB-stability criterion and the phonon stability criterion must both be satisfied. This ensures stability with respect to all quasi-uniform perturbations (CB stability) and bounded displacement perturbations of all wavelengths (phonon stability).

2.5. Selection of equilibrium paths corresponding to proper martensitic transformations

The numerical solution of the equilibrium equations (2.8) yields a large number of equilibrium paths. Even after the exclusion of the unstable branch segments, a significant number of stable path segments are found within the loading range of interest. The question is which of this multitude of stable path segments found in the neighborhood of the high-symmetry austenite phase are candidates for a *proper* (reversible) martensitic transformation, such as those found in SMAs.

As defined by Elliott et al. (2002), a *proper* martensitic transformation is one where the space (symmetry) group of the martensite phase is a proper sub-group of the austenite's space group (all other martensitic transformations are called *reconstructive*). According to Bhattacharya et al. (2004), it is *necessary* that a martensitic transformation be proper in order for it to be *reversible*. As stated in Bhattacharya et al. (2004):

> "In these cases [i.e., proper martensitic transformations], the energy barrier to lattice-invariant shear is generically higher than that pertaining to the phase change and, consequently, transformations of this type can occur with virtually no plasticity. Irreversibility is inevitable in all other martensitic transformations [i.e., reconstructive martensitic transformations], where the energy barrier to plastic deformation (via lattice-invariant shears [defined below], as in twinning or slip) is no higher than the barrier to the phase change itself."

Thus, to determine which of the candidate martensite phases—discovered in this work—correspond to possible *proper* martensitic transformations, we employ the concept of the *maximal Ericksen–Pitteri neighborhood* (max EPN) which is a

[4] The acoustic phonons at $\mathbf{k}=\mathbf{0}$ and $q=1,2,3$ have been excluded since their frequencies are identically zero and correspond to the rigid-body translation modes of the crystal.

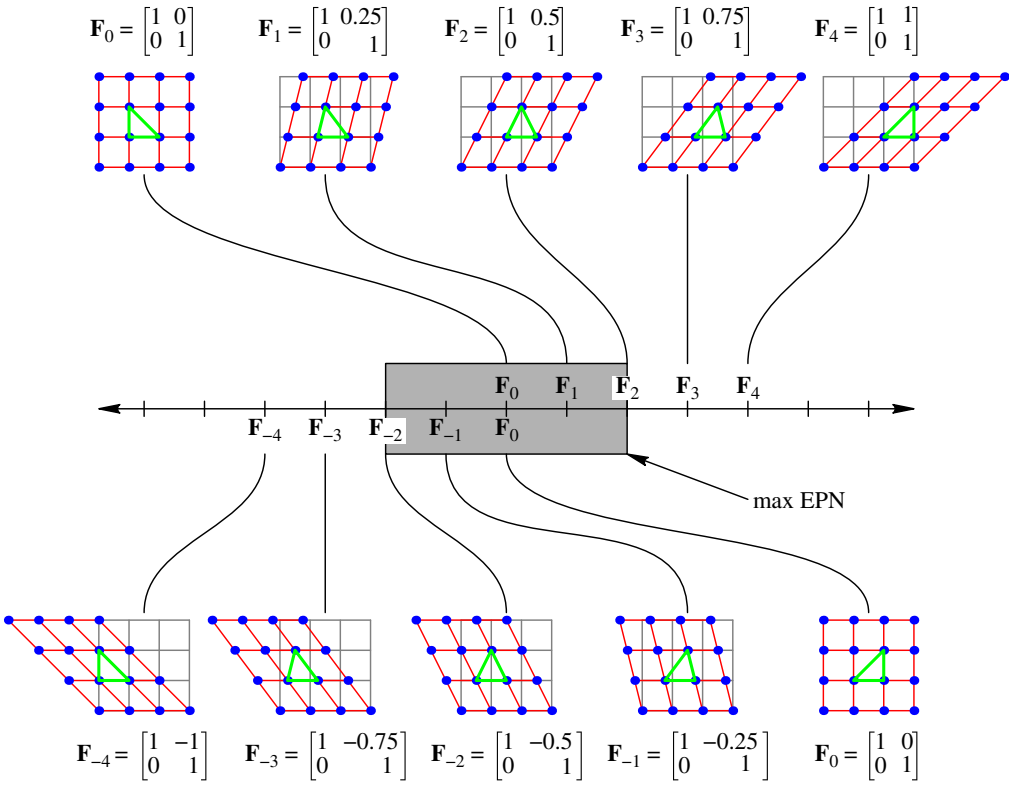

Fig. 2. Schematic of the maximal Ericksen–Pitteri neighborhood.

kinematic idea that allows one to find the lattice deformations that are *closest* to the austenite phase (Ericksen, 1980; Pitteri, 1984).[5]

The max EPN, centered on the austenite configuration $\mathbf{F}_0$, is schematically illustrated in Fig. 2, using a two-dimensional lattice for simplicity. Assuming that the high symmetry austenite phase is the square lattice configuration shown in the top left (bottom right) of Fig. 2, it may be deformed by continuous simple shear to an identical square lattice as shown in the top right (bottom left) of Fig. 2. The square lattices, related by this *lattice-invariant shear* transformation and characterized by $\mathbf{F}_0$, $\mathbf{F}_4$, and $\mathbf{F}_{-4}$, are indistinguishable from a crystallographic viewpoint. During the deformation process leading from $\mathbf{F}_0$ to $\mathbf{F}_4$ ($\mathbf{F}_0$ to $\mathbf{F}_{-4}$) one traverses the intermediate deformation $\mathbf{F}_2$ ($\mathbf{F}_{-2}$), which corresponds to a lattice configuration *half-way* between the reference and final square lattices.

Suppose, the martensite equilibrium branch is *close* to the parent phase, i.e., between $\mathbf{F}_{-2}$ and $\mathbf{F}_2$. Then, upon reverse transformation the martensite phase will likely return to the original parent austenite phase $\mathbf{F}_0$. This corresponds to a proper martensitic transformation such as those observed in SMAs. If, on the other hand, the martensite phase exists between $\mathbf{F}_2$ and $\mathbf{F}_4$ ($\mathbf{F}_{-2}$ and $\mathbf{F}_{-4}$), then upon reverse transformation it will more likely revert to the crystallographically identical (lattice-invariant sheared) austenite phase $\mathbf{F}_4$ ($\mathbf{F}_{-4}$). Thus, deformations strictly between $\mathbf{F}_{-2}$ and $\mathbf{F}_2$ constitute the maximal EPN of the parent phase (high symmetry austenite configuration $\mathbf{F}_0$). The interested reader is referred to Conti and Zanzotto (2004), Bhattacharya et al. (2004), and the references cited therein, for a further elaboration of these ideas. The discussion above and that found in Conti and Zanzotto (2004) are given in the context of simple Bravais lattices, while EPNs of multilattices are discussed by Pitteri and Zanzotto (2002) and in Pitteri (2003a, b). It seems that an investigation of how these neighborhoods depend on the choice of multilattice description for a crystal is not available. We do not attempt to address this important issue, but instead base all EPN calculations on the fixed 4-lattice as described in detail in Appendix A.1.

Lattice-invariant shear transformations are a key component of the max EPN idea. These transformations (plus the rigid-body rotations that map the lattice to itself) are characterized by deformations $\mathbf{F}_s$ with $\det(\mathbf{F}_s)=1$. With respect to a mixed basis of lattice and reciprocal lattice vectors ($\mathbf{g}_i$ and $\mathbf{g}^j$), one has $\mathbf{F}_s=(F^i{}_j)\mathbf{g}_i\mathbf{g}^j$ where $F^i{}_j$ is a 3×3 matrix with integer components such that $\det(F^i{}_j)=1$. These matrices belong to an infinite group, called the group of special linear transformations of degree three over the field of integers $\mathbb{Z}$ and denoted by $SL(3,\mathbb{Z})$.

For a multilattice crystal with atomic positions $\mathbf{x}[^{\ell}_{\alpha}]$, a lattice-invariant sheared configuration $\overset{\star}{\mathbf{x}}[^{\ell}_{\alpha}]$ is defined as one that satisfies the relation $\overset{\star}{\mathbf{x}}[^{\ell}_{\alpha}]=\mathbf{x}[^{\ell'}_{\alpha}]$ where $(\ell')^i=F^i{}_j\ell^j$ for some $\mathbf{F}_s$. Generally, such a configuration may be obtained by the

[5] It is straightforward to show that every configuration (strictly) within the max EPN has a space group that is a proper sub-group of the space group associated with the max EPN's center configuration (i.e., the space group of the austenite configuration).

application of an $\mathbf{F}_s$ *and* sublattice shifts $\mathbf{s}_s[\alpha]$ to the configuration $\mathbf{x}[^{\ell}_{\alpha}]$. That is,

$$\overset{\star}{\mathbf{x}}\begin{bmatrix}\ell\\ \alpha\end{bmatrix} \equiv \mathbf{F}_s \cdot \mathbf{x}\begin{bmatrix}\ell\\ \alpha\end{bmatrix} + \mathbf{s}_s[\alpha] = \mathbf{x}\begin{bmatrix}\ell'\\ \alpha\end{bmatrix}. \tag{2.16}$$

Additionally, the formulation adopted here uses the right stretch tensor $\mathbf{U}$ as the independent variables for lattice deformations. In general, the lattice-invariant shear transformation will not produce another deformed configuration that can be represented with a symmetric tensor $\mathbf{U}$ as required by Eq. (2.3). However, the polar decomposition theorem may be applied to the resulting deformation tensor and an equivalent, rigidly rotated, representation can be identified that does fit the prescription of Eq. (2.3). Thus,

$$\overset{\star}{\mathbf{x}}\begin{bmatrix}\ell\\ \alpha\end{bmatrix} = \overset{\star}{\mathbf{R}} \cdot \overset{\star}{\mathbf{U}} \cdot \left(\mathbf{X}\begin{bmatrix}\ell\\ \alpha\end{bmatrix} + \overset{\star}{\mathbf{S}}[\alpha]\right). \tag{2.17}$$

The quantities $\overset{\star}{\mathbf{R}}$, $\overset{\star}{\mathbf{U}}$, and $\overset{\star}{\mathbf{S}}[\alpha]$, may be determined by using the relation $\mathbf{x}[^{\ell}_{\alpha}] = \overset{o}{\mathbf{U}} \cdot (\mathbf{X}[\ell] + \mathbf{P}[\alpha] + \overset{o}{\mathbf{S}}[\alpha])$ in Eqs. (2.16) and (2.17) and eliminating the $\mathbf{s}_s[\alpha]$ to obtain

$$\overset{\star}{\mathbf{R}} \cdot \overset{\star}{\mathbf{U}} = \mathbf{F}_s \cdot \overset{o}{\mathbf{U}}, \tag{2.18}$$

$$\overset{\star}{\mathbf{S}}[\alpha] = (\overset{o}{\mathbf{U}})^{-1} \cdot (\mathbf{F}_s)^{-1} \cdot \overset{o}{\mathbf{U}} \cdot (\mathbf{P}[\alpha] + \overset{o}{\mathbf{S}}[\alpha]) - \mathbf{P}[\alpha]. \tag{2.19}$$

To determine if the configuration of a given equilibrium path (characterized by the quantities $\overset{o}{\mathbf{U}}$ and $\overset{o}{\mathbf{S}}[\alpha]$) is inside the max EPN of the reference austenite structure, the lattice-invariant shear $\mathbf{F}_s$ is chosen such that $\overset{\star}{\mathbf{U}}$ minimizes the norm[6]

$$\|\overset{\star}{\mathbf{U}} - \mathbf{I}\| \equiv |\overset{\star}{\lambda}_1 - 1| + |\overset{\star}{\lambda}_2 - 1| + |\overset{\star}{\lambda}_3 - 1|, \tag{2.20}$$

where $\overset{\star}{\lambda}_i$ are the principal stretches of $\overset{\star}{\mathbf{U}}$. If the originally obtained configuration is not a minimizer (i.e., $\overset{\star}{\mathbf{U}} \neq \overset{o}{\mathbf{U}}$), then it lies outside the max EPN. If it is a minimizer, then one must further determine if it falls on the boundary of the max EPN. Thus, only those stable equilibrium configurations that are found to exist *strictly* inside the max EPN are identified as the martensite phase of a possible proper PT.

The above minimization is a discrete optimization problem for which the authors are not aware of an efficient numerical method. Thus, in this work the numerical calculations pertaining to the investigation of whether a particular equilibrium configuration is in the max EPN of the austenite reference configuration are based on a large, but finite, set of lattice-invariant shear deformations generated by

$$\mathbf{F}_s = (\mathbf{F}_i)^I \cdot (\mathbf{F}_j)^J \cdot (\mathbf{F}_k)^K \cdot (\mathbf{F}_l)^L \cdot (\mathbf{F}_m)^M \cdot (\mathbf{F}_n)^N, \tag{2.21}$$

where the exponents $-6 \leq I,J,K,\ldots,N \leq 6$ are integers and the deformations $\mathbf{F}_i$ (with $1 \leq i,j,k,\ldots,n \leq 6$) are simple shears that shift by one atomic distance neighboring planes of atoms along the lattice directions, namely:

$$\mathbf{F}_1 = \mathbf{I} + \mathbf{g}_2\mathbf{g}^3, \quad \mathbf{F}_2 = \mathbf{I} + \mathbf{g}_3\mathbf{g}^1, \quad \mathbf{F}_3 = \mathbf{I} + \mathbf{g}_1\mathbf{g}^2,$$

$$\mathbf{F}_4 = (\mathbf{F}_1)^T, \quad \mathbf{F}_5 = (\mathbf{F}_2)^T, \quad \mathbf{F}_6 = (\mathbf{F}_3)^T. \tag{2.22}$$

It is conjectured that this set of more than 4.8 million elements of $SL(3,\mathbb{Z})$ is sufficient to ensure that the correct minimizing element is obtained for the situations encountered in this work.

3. Results

The presentation of results starts with the investigation of the equilibrium paths for the stress-free prefect crystal, thus finding which equilibrium configurations, in addition to the high symmetry reference cubic B2 (CsCl) structure, are observable within the temperature range of interest. The equilibrium paths of the perfect crystal stressed along the $[1\ 1\ 0]_{B2}$ direction and at a fixed temperature $\theta = 1.2$ are presented next. The results of the equilibrium path calculations obtained via the continuation methods presented in the previous section are simplified first by considering only their stable segments. Subsequently, and upon making use of lattice-invariant shear transformations to establish the paths within the max EPN of the stress-free B2 austenite phase, those equilibrium paths that are candidates for a *proper* martensitic transformation are identified. Guided by these results, further calculations are performed at different temperatures and along a different load direction to find the corresponding stress-induced martensitic phase transformations. The section ends with an investigation of the influence of the loading device.

A general comment on crystal structure nomenclature is in order at this point. The space group of each equilibrium configuration is found from the coordinates of the atoms and the lattice parameters of the unit cell with the help of *Cerius*[2] software by *Accelrys*. However, the space group does not uniquely characterize the crystal structure, e.g., monoatomic as well

[6] Since all norms in the finite-dimensional (six) space of deformations are equivalent, the present choice is adopted for computational convenience.

as poly-atomic crystals can share the same symmetry group. Thus to be more specific, the *Strukturbericht Designation* of the zero-stress configuration is used to further specify the crystal structure of the corresponding equilibrium branches. For the crystals investigated here, their *Strukturbericht Designation* names always start with a B (since it is a bi-atomic crystal with 50–50 composition) followed by a number, e.g., B2, B11, B19, B33, etc. Another nomenclature used in crystallography is the *Prototype Designation*, which consists of the chemical name of a prototype compound that exists with that structure, e.g., CsCl, αIrV, etc. For more information, see the *Crystal Lattice Structures Web page*, http://cst-www.nrl.navy.mil/lattice/, provided by the Center for Computational Materials Science of the United States Naval Research Laboratory. In this way the B2 *Strukturbericht Designation* is equivalent to the CsCl *Prototype Designation*. If a *Strukturbericht Designation* is not available, a *Prototype Designation* is used in this work. Unfortunately, our calculations can sometimes result in bi-atomic crystal structures for which we have not been able to identify either a *Strukturbericht Designation* or a *Prototype Designation*. In such a case, only the space group name is provided.

Finally, a note about the presentation of results. The reference configuration chosen is the austenite B2 phase at zero stress and reference temperature $\theta = 1$. In the graphs that follow, the potential energy per unit reference volume $\widetilde{\mathcal{E}}$ and the applied stress along the **N** direction, Σ, are given in dimensionless form with respect to C_{11}—the 1111 component, with respect to the B2 cubic axes, of the elastic modulus (Voigt notation) at the reference configuration, i.e., $C_{11} \equiv [\partial^2 \widetilde{W}/\partial U_{11}\partial U_{11}]_{(\mathbf{U}=\mathbf{I},\mathbf{S}=\mathbf{0},\theta=1)}$. In the same graphs, the stretch along the **N** direction, λ, is work-conjugate to Σ (recall $\lambda \equiv \mathbf{N}\cdot\mathbf{U}\cdot\mathbf{N}$ according to Eq. (2.7)), and θ is the dimensionless temperature.

3.1. Stress-free, temperature-induced transformations

The paths obtained by solving the equilibrium equation (2.8) for the special case of zero stress (i.e., by using the dimensionless temperature θ as the load parameter with $\Sigma = 0$) are plotted as the largest principal stretch, $\lambda_{\max}$, versus dimensionless temperature θ in Fig. 3. The paths are obtained by a methodical search, which starts by identifying all bifurcation points on the *principal* (B2) path and following all the emerging *secondary* equilibrium paths. All bifurcation points on the secondary paths are identified and their emerging *tertiary* branches are followed and so on until no new paths are found within the temperature range of interest. Bifurcation and limit points are depicted respectively by open and filled circles. Stable equilibrium path segments are depicted by solid lines while unstable segments of these paths are depicted by broken lines. A magnified view of the many bifurcated equilibrium paths emerging from the principal branch is shown in the inset of Fig. 3.

Several crystal structures are found for the bifurcated equilibrium paths: one tetragonal ($L1_0$), two orthorhombic (B19 and αIrV), and one monoclinic (P2/m). Multiple symmetry related paths exist for each of these structures (three $L1_0$ tetragonal

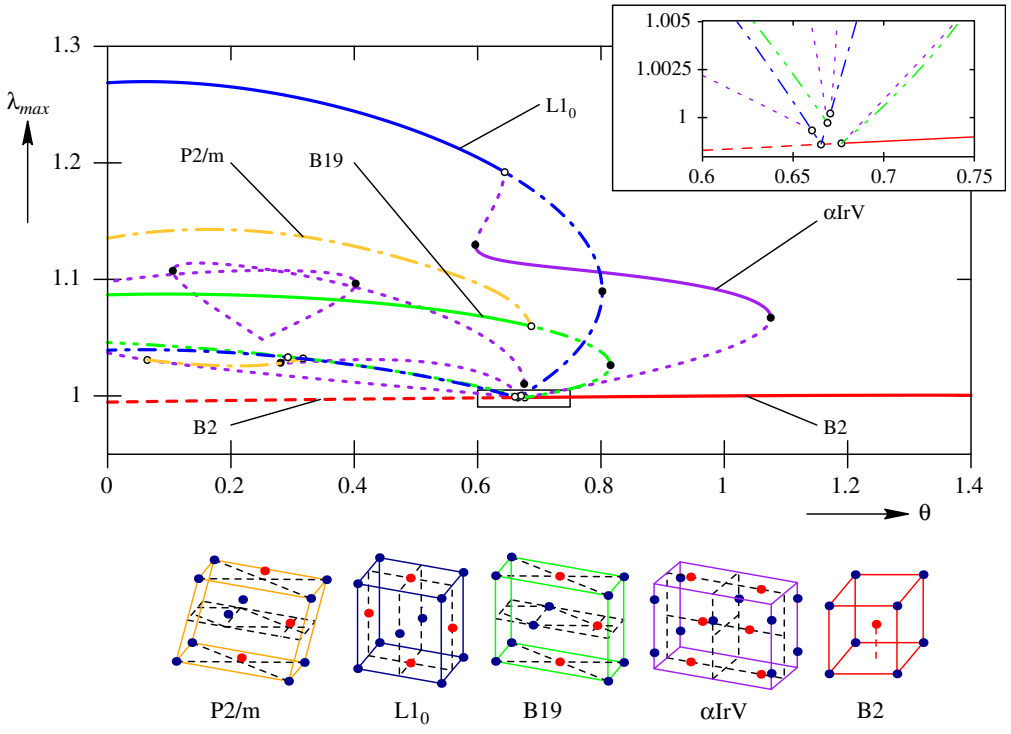

Fig. 3. Largest principal stretch $\lambda_{\max}$, with respect to the reference configuration, versus dimensionless temperature θ for the stress-free bifurcated equilibrium paths connected to the B2 austenite phase and their crystal structures. The stable portion of each equilibrium path is depicted by a solid line.

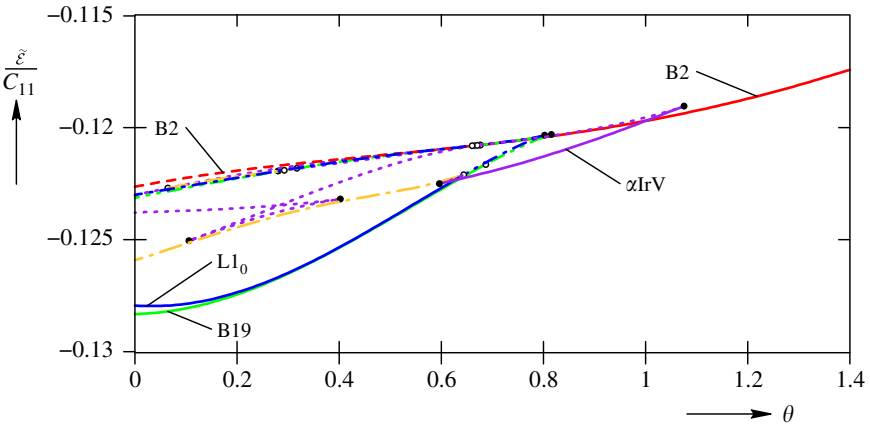

Fig. 4. Dimensionless energy density versus dimensionless temperature for the stress-free, bifurcated equilibrium paths connected to the B2 austenite phase. The stable portion of each equilibrium path is depicted by a solid line.

paths, six each of the αIrV and B19 orthorhombic paths, and six[7] P2/m monoclinic paths); however, for the particular quantities plotted herein all symmetry related paths collapse to a single curve. Of the four structures discovered, only the αIrV, B19, and $L1_0$ equilibrium branches have stable portions. The tetragonal ($L1_0$) lattice does not involve internal shifts, resulting from a simple affine (Cauchy) deformation of the B2 crystal, while the other three do involve internal shifts. Moreover, the stable αIrV phase appears in the higher temperature range (approximately $0.6 \le \theta \le 1.1$), while the B19 and $L1_0$ are stable at lower temperatures (approximatively $\theta \le 0.7$ and $\theta \le 0.65$, respectively). As expected the B2 austenite phase is stable for high temperatures and unstable for low temperatures. Also, it is interesting to note that $L1_0$ and B19 are common SMA martensite structures (Bhattacharya, 2003), and the αIrV structure has previously been observed (although not mentioned by name) in the numerical computations of Ding et al. (2006).

We recognize that the equilibrium paths shown in Fig. 3 are all the paths in the temperature range $0 \le \theta \le 1.4$ that are ultimately connected to the austenite phase B2. If other, isolated equilibrium paths exist in the above temperature range or if paths are connected to the principal branch at a bifurcation point outside the temperature range, our search method cannot find them. Notice that all stable equilibrium paths are parts of secondary branches, emerging from the principal solution, and hence their space group is a proper subgroup of the cubic (B2) lattice's. Consequently, these stable branches belong to the max EPN of the B2 austenite and are reversible martensitic transformation candidates. Similar calculations were reported in Elliott et al. (2006a) for the stress-free, temperature-induced transformations of a bi-atomic perfect lattice (with somewhat different pair potentials), where stable bifurcated equilibrium solutions with tetragonal $L1_0$ and orthorhombic B19 structure were found, but not the orthorhombic αIrV. The reason is that the stable part of this equilibrium branch appears only after one follows it to sufficiently high temperatures (near $\theta = 1.1$) where a limit point appears and the unstable path restabilizes for lower temperatures.

For the stress-free equilibrium paths shown in Fig. 3, their dimensionless energy densities $\tilde{\varepsilon}/C_{11}$ versus the dimensionless temperature θ are plotted in Fig. 4. The tetragonal $L1_0$ phase is never the minimum energy configuration for any temperature. At high temperatures, the B2 lattice is stable and has the lowest energy. B2 and αIrV have an energy crossing at about $\theta = 1$, while αIrV and B19 have an energy crossing at about $\theta = 0.6$. These represent temperatures where equilibrium transformations could occur, if energy barriers between the parent and daughter phases are neglected. If they are not neglected, the parent phase (upon further cooling or heating) becomes metastable until it looses local stability altogether. If a transformation occurs at the end point of a stable equilibrium path, a dynamic jump from the higher to the lower energy path will occur. Thus, transformations associated with a cool-then-heat cycle will exhibit a temperature hysteresis. According to the results in Fig. 4, the relative positions of the stable portions of the energies for the B2, αIrV, and B19 paths indicate the possibility of a hysteretic loop in the martensitic transformations between B2 and αIrV and also in the transformation between αIrV and B19. Two-stage MTs are found in many SMAs such as AuCd and NiTi, although the particular crystal structures are different.

3.2. *Stress-induced transformations at a fixed temperature ($\theta = 1.2$) with $[1\ 1\ 0]_{B2}$ Biot uniaxial loading*

The results of the previous subsection showed that the model developed is capable of exhibiting multiple proper temperature-induced MTs that qualitatively capture the corresponding behavior of real SMAs. However, stress-induced MTs are an integral part of SMA behavior. Thus, the existence of such MTs predicted by the model is investigated.

According to Fig. 3, at temperature $\theta = 1.2$, the only stress-free equilibrium path found is the stable part of the B2 austenite path. Now we consider whether, at this temperature, the application of stress can lead to a reversible martensitic transformation

[7] The P2/m paths bifurcate symmetrically from the B19 paths and each symmetric path corresponds to two conventional variants of the monoclinic phase. Thus, we do, in fact, obtain all 12 variants of the monoclinic structure.

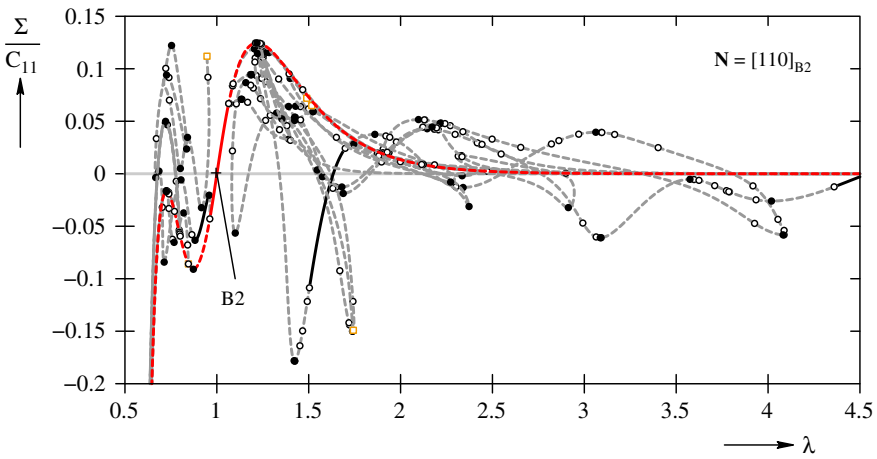

Fig. 5. Dimensionless stress versus conjugate stretch for $[1\ 1\ 0]_{B2}$ Biot loading showing all bifurcated secondary equilibrium paths that are connected to the principal B2 path. Stable segments are depicted in solid lines.

by applying a uniaxial Biot loading of magnitude Σ along the $[1\ 1\ 0]_{B2}$ direction, i.e., along $\mathbf{N}=(\mathbf{G}_1+\mathbf{G}_2)/(\sqrt{2}a)$—where $a=\|\mathbf{G}_1\|$ is the reference lattice spacing.

Following all the bifurcated equilibrium paths emerging from the principal B2 solution results in a highly tangled set of equilibrium paths. The dimensionless stress Σ/C_{11} versus conjugate stretch λ results for only the secondary equilibrium paths emerging from the principal B2 path are depicted in Fig. 5. Bifurcation points where the symmetry of the emerging new equilibrium path increases, i.e., points where a reconstructive equilibrium path emerges, are depicted by open squares. It should also be noted that such paths are not followed because they do not lead to proper martensitic transformations.

The complexity of the picture is due to the fact that there are 18 secondary bifurcated paths (emerging from B2), with a total of 164 critical points on them. For symmetry reasons only 142 distinct critical points appear in Fig. 5. The equilibrium paths were followed to large stretches ($\lambda>4.5$) to ensure that no stable paths, ultimately connected to B2, were missed. Three stable segments are found in the secondary bifurcated paths emerging from B2, one segment for negative Σ and stretch ratios at about $\lambda=0.9$, a second segment crossing the zero stress axis at about $\lambda=1.7$, and a third segment crossing the axis about $\lambda=4.5$. The first stable secondary bifurcation path segment (with $\lambda<1$) is a distorted version of the αIrV crystal structure found in the previous stress-free calculations, while the other two stable secondary bifurcation path segments (with $\lambda>1$) are lattice-invariant shear deformations of the B2 crystal.

Of course, the full investigation of the crystal's behavior requires the subsequent calculations of the tertiary and quartiary paths. While they were in fact calculated, one can easily appreciate that the graph of the full set of equilibrium paths is hopelessly dense for presentation and is thus not shown. It suffices to state that there are 135 tertiary bifurcated paths (emerging from all the secondary branches) and more than 114 quartiary bifurcated paths (emerging from all the tertiary branches). From these calculations 22 stable segments, with respect to both the CB and phonon criteria, are found. The stable segments of the dimensionless stress Σ/C_{11} versus stretch λ curves thus obtained, each labeled by its symmetry group, are shown in Fig. 6. For the paths that include zero stress, their names and corresponding crystal structures are also shown.

Not all of these 22 stable equilibrium paths are candidates for reversible martensitic transformations, and culling out those paths with configurations outside the max EPN leaves the paths depicted in Fig. 7.

Notice from Fig. 7 that besides the principal branch, three stable equilibrium paths exist that include zero stress: two with a structure in the C2/m space group and one with a B33 structure. The B33 structure is important in B2 to B1 reconstructive PTs (Stokes et al., 2004) and has recently become of interest for NiTi (Huang et al., 2003a). It is interesting that our model also predicts this phase to be stable. In addition, three other stable equilibrium paths (two in the tensile regime and one in the compressive regime) exist, which do not include zero stress, yet are closer to the principal path. From the two stable paths in tension, one belongs to the C2/m space group and one to the P2/m group, while the stable (strictly) compression path belongs to the C2/m space group. These three equilibrium paths are stress-distorted versions of the αIrV structure found in the stress-free calculations in Fig. 7 (for lower temperatures these equilibrium paths go through zero stress, at which point they have an αIrV structure, as will be seen in the next subsection).

Finally, from kinematic considerations, one can argue that the stable path which has a B33 structure at zero stress and the two stable paths which at zero stress belong to the C2/m group are on the boundary of the max EPN of the B2 configuration. Indeed, as seen in Fig. 8, the C2/m and B33 structures can be considered to be exactly *half-way* along a lattice-invariant shear deformation of the B2 structure. In Fig. 8 the solid lines indicate the B33 and C2/m lattice cells as well as the original B2 lattice cells. Thus, equilibrium configurations with the C2/m or B33 lattice structure are equally close to two separate B2 structures which differ by a lattice-invariant shear. Accordingly, these paths are excluded from being reversible martensitic transformation candidates, since they are not strictly inside the max EPN. This leaves only three stable equilibrium paths: two in tension and one in compression, as shown in Fig. 9(a).

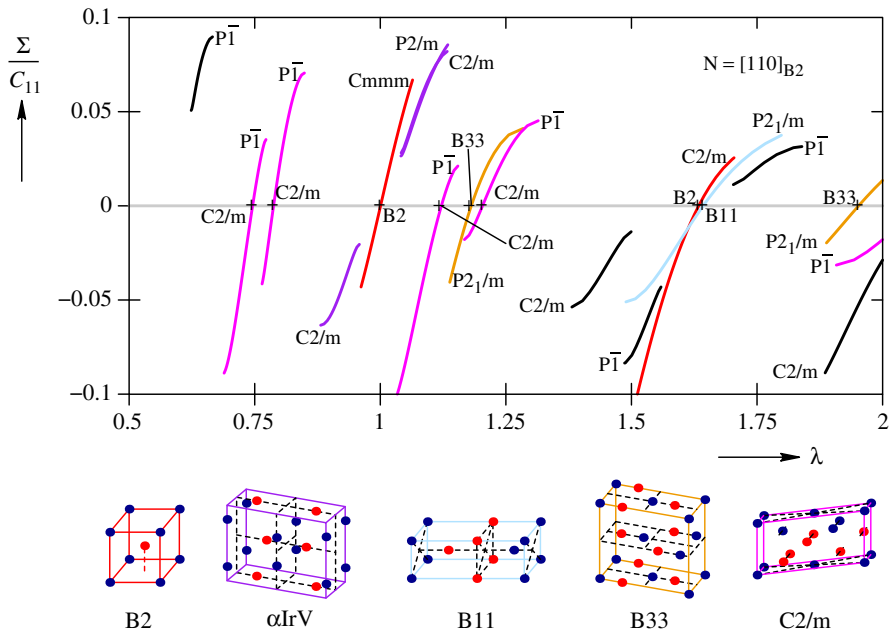

Fig. 6. Dimensionless stress versus conjugate stretch graph for all the stable equilibrium paths under $[1\ 1\ 0]_{B2}$ Biot loading, each labeled by its symmetry group. For the paths going through zero stress, their names and corresponding crystal structures are also depicted.

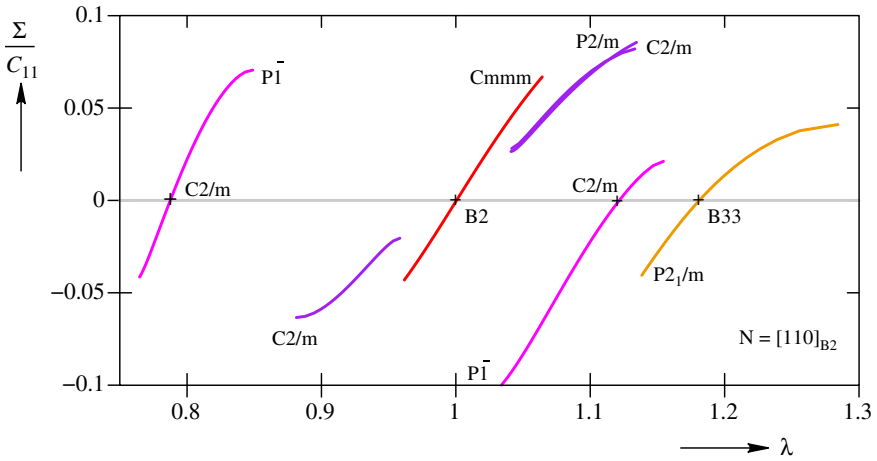

Fig. 7. Dimensionless stress versus conjugate stretch graph showing only the stable equilibrium paths under $[1\ 1\ 0]_{B2}$ Biot loading which are not outside the max EPN of the B2 configuration.

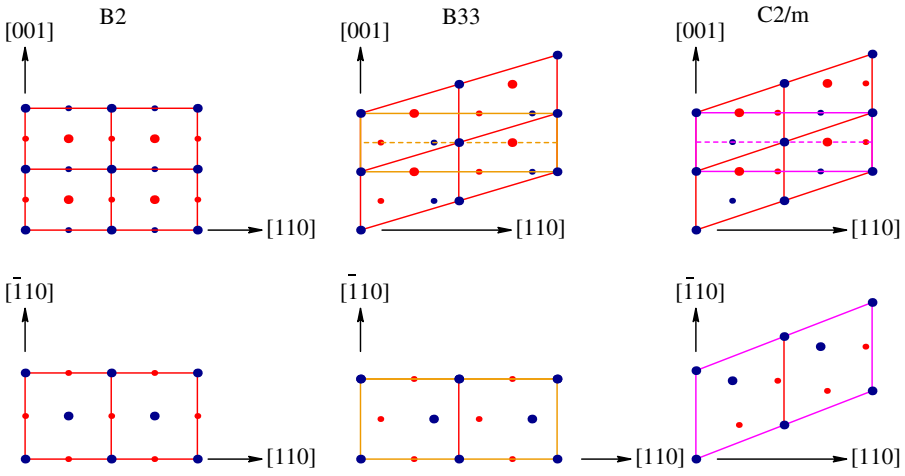

Fig. 8. Schematic showing why B33 and C2/m lattice structures are on the boundary of the max EPN of B2.

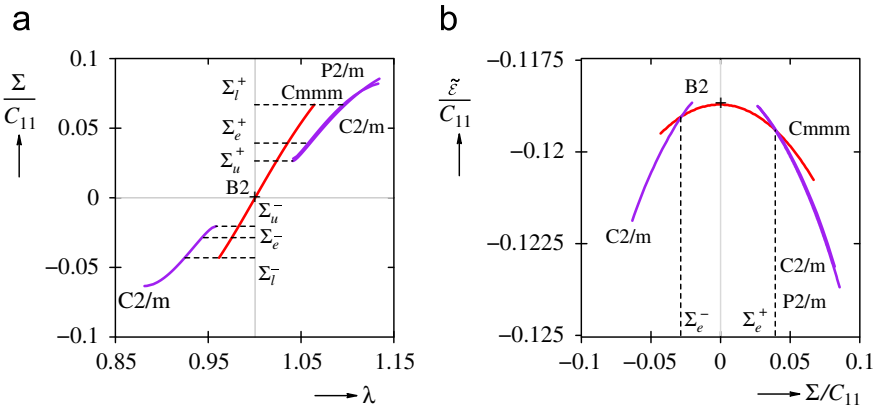

Fig. 9. Dimensionless stress versus conjugate stretch graphs for the martensite equilibrium paths in (a) and corresponding dimensionless energy density versus dimensionless stress shown in (b) for $[1\ 1\ 0]_{B2}$ uniaxial Biot loading at $\theta = 1.2$.

The existence of three different martensite branches in Fig. 9, can be explained as follows: these equilibrium paths are stress-distorted versions of the αIrV structure found in the stress-free calculations of Fig. 7. Since αIrV is an orthorhombic lattice, six different variants are energetically equivalent at zero stress. When a $[1\ 1\ 0]_{B2}$ uniaxial Biot load is applied, one obtains three inequivalent sets of loaded configurations, each containing two energetically equivalent configurations due to the symmetry of the variants relative to the loading direction. Consequently three distinct paths appear in the stress–stretch graph shown in Fig. 9. This kinematic observation also shows that no martensite αIrV branch has been missed.

The results in Fig. 9(a) show the possibility of the pseudoelastic, hysteretic behavior of a perfect B2 crystal. In the neighborhood of zero stress, only the high symmetry austenite equilibrium path (elastically distorted version of B2 lattice structure) is stable. As the stress increases, in tension (or compression), it reaches a value $\Sigma_l^+ = 0.067$ (or $\Sigma_l^- = -0.043$) where a stable austenite path no longer exists and the only stable paths within the max EPN of the austenite configuration are the martensite paths (the distorted versions of the αIrV lattice structure). Thus, transformation to the martensite phase is to be expected. Upon unloading of the martensite phase, the stress in tension (compression), reaches a value $\Sigma_u^+ = 0.026$ ($\Sigma_u^- = -0.020$) where a stable martensite path no longer exists and the crystal returns to the stable austenite path. It is worth noticing that a tension/compression asymmetry exists, i.e., $\Sigma_l^+ \neq -\Sigma_l^-$ and $\Sigma_u^+ \neq -\Sigma_u^-$. This is characteristic of real SMAs (Gall et al., 1999) and is a feature often missing from SMA material models. Here, the underlying atomic nature of our model captures the tension/compression asymmetry in a natural way and without special effort.

The energetic counterpart of the austenite-to-martensite transformation is shown in Fig. 9(b), plotted against the dimensionless stress. In the neighborhood of zero stress, the austenite phase has the lowest energy density $\tilde{\mathcal{E}}$. Upon loading in tension (compression) one reaches a critical stress $\Sigma_e^+ = 0.039$ ($\Sigma_e^- = -0.029$) beyond which the martensite phase has the lowest energy, thus indicating the possibility of transformation from an equilibrium thermodynamics standpoint (where the "e" subscript in the corresponding transformation stress symbol denotes the equilibrium value). This equilibrium value also exhibits the tension/compression asymmetry.

3.3. *Stress-induced transformations at other temperatures*

Having established the existence of a stress-induced proper martensitic transformation at $\theta = 1.2$, attention is next focused on finding the stress versus stretch equilibrium diagrams, analogous to Fig. 9, at different temperatures, keeping the same $[1\ 1\ 0]_{B2}$ Biot loading. The search approach used for $\theta = 1.2$, which followed all the bifurcated equilibrium paths emerging from the austenite principal path, is rather time consuming. Fortunately, one can be aided by the final results of Fig. 9 to construct, by continuity arguments, similar diagrams for other temperatures. The idea, similar to that used by Healey and Miller (2007), is to use selected equilibrium points on the relevant martensite branches from Fig. 9, fixing the stress, and then follow these equilibrium paths as the temperature is varied. Once a desired temperature is reached, the paths are followed again for variable stress, thus establishing isothermal stress versus stretch graphs at the new temperatures.

The results in Fig. 10 show the $[1\ 1\ 0]_{B2}$ stretch ratio versus temperature equilibrium paths for the three different martensite branches for several stress levels. Specifically, Fig. 10(a, b) correspond to the compressive and tensile, respectively, branches of Fig. 9 with C2/m symmetry and Fig. 10(c) corresponds to the tensile P2/m branch of Fig. 9.

Starting at selected equilibrium points in Fig. 10, the isothermal stress versus stretch and energy versus stress diagrams for the austenite and martensite branches were found at temperatures $\theta = 0.95, 1.05$, and 1.15 as shown in Fig. 11. Notice that for the two lower temperatures, stable austenite and martensite branches exist at zero stress, while for the highest temperature only the austenite branch is stable at zero stress. As expected, for the lowest temperature $\theta = 0.95$ the austenite branch's energy near zero stress is above the corresponding energy of the martensite branch. As the temperature increases the situation reverses itself. For temperatures $\theta > 1$, the global energy minimum for zero stress corresponds to the austenite phase, but as the applied stress increases, the martensite phases have less energy than the austenite one.

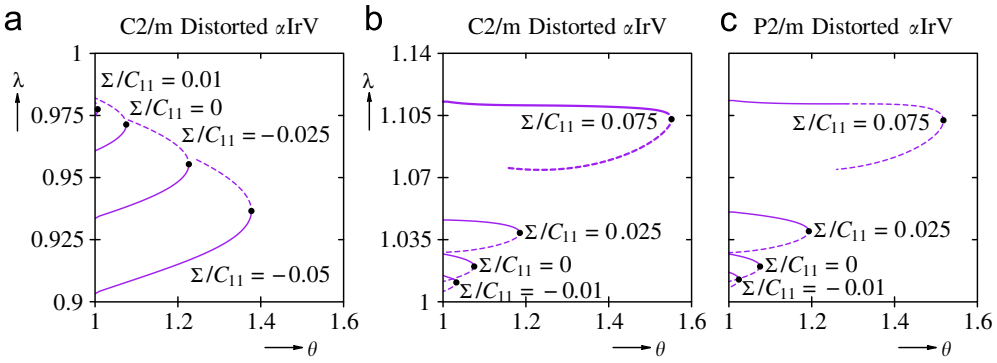

Fig. 10. Stretch ratio versus temperature at different $[1\ 1\ 0]_{B2}$ Biot stress levels for the three sets of variants of the αIrV crystal structure: (a) compression C2/m variants, (b) tension C2/m variants, and (c) tension P2/m variants.

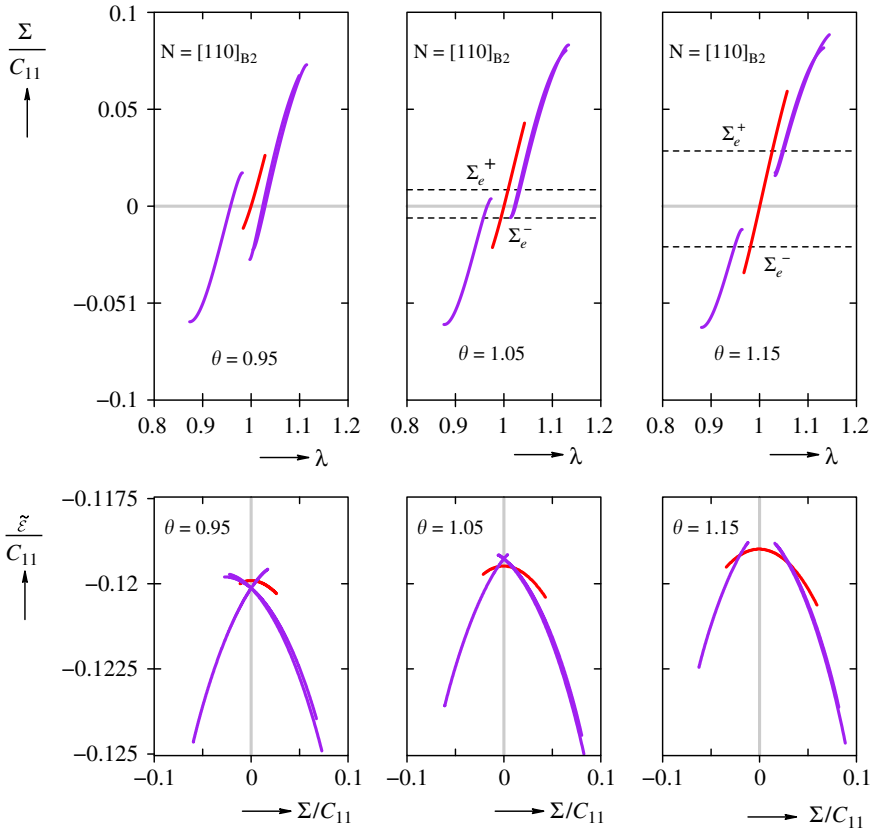

Fig. 11. Stress versus stretch ratio paths of austenite and martensite under $[1\ 1\ 0]_{B2}$ Biot loading for various temperatures.

At each temperature, the stresses at which energies intersect are shown as Σ_e. One can see that $|\Sigma_e^{\pm}|$ increases with θ, in qualitative agreement with the stress-induced transformation behavior of known SMAs (Shaw and Kyriakides, 1995). Using T_{ref}=300 K and C_{11}=80 GPa, the current perfect crystal model gives an effective Clausius–Clapeyron slope of $|d\Sigma_e^{\pm}/dT| \approx 53$ MPa/K, which is higher than usually measured (2–12 MPa/K are typical experimental values obtained from polycrystalline samples). It should be noted that the Clausius–Clapeyron slope is likely to be sensitive to the EIP's parameters. Moreover, it is also reasonable to expect that the predicted value for the Clausius–Clapeyron slope is sensitive to geometric and loading imperfections.[8] However, predictive quantitative matching of experimental values measured from real polycrystalline samples would require more sophisticated multiscale models that can account for the influence of defects

[8] Imperfection sensitivity, such as is well-known in certain shell structures (Thompson and Hunt, 1984), does not apply here because the Clausius–Clapeyron slope is determined by states of the system which are typically finitely removed from its bifurcation points. However, because of the density of (stable and unstable) equilibrium solutions in the neighborhood of the configurations of interest, sensitivity to such imperfections can be expected for the Clausius–Clapeyron slope.

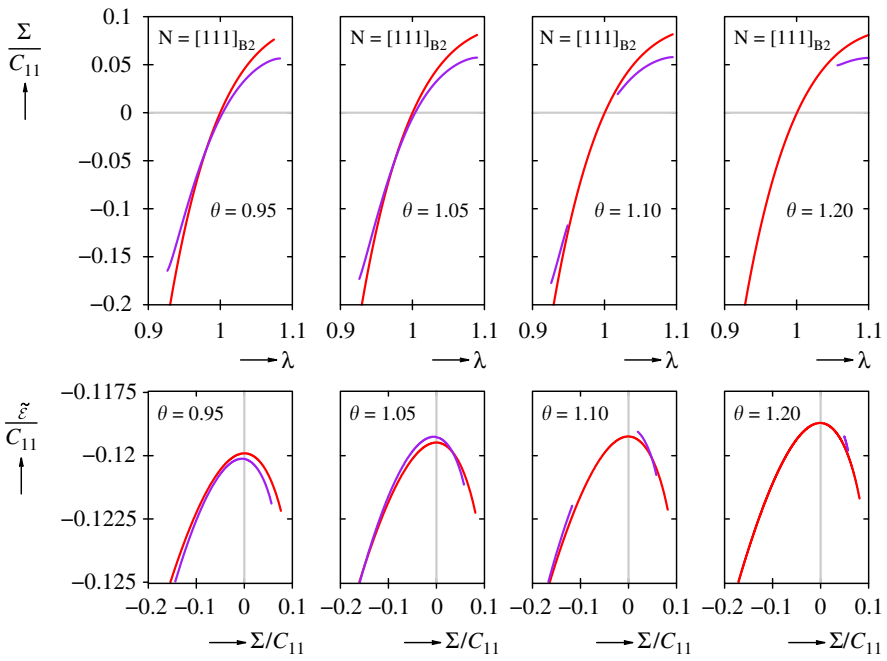

Fig. 12. Stress versus stretch ratio paths of austenite and martensite under $[1\ 1\ 1]_{B2}$ Biot loading for various temperatures.

(large imperfections) such as vacancies, precipitates, dislocations, and grain boundaries, as well as the well-known effects associated with alloy composition (Otsuka and Wayman, 1998).

3.4. Stress-induced transformations for other loading directions

A similar (and equally lengthy) procedure was followed for $[1\ 1\ 1]_{B2}$ Biot loading, i.e., for $\mathbf{N}=(\mathbf{G}_1+\mathbf{G}_2+\mathbf{G}_3)/(\sqrt{3}a)$. The corresponding results are shown in Fig. 12. There are several interesting differences between the two loading situations: the first difference is that unlike the $[1\ 1\ 0]_{B2}$ Biot loading, for the $[1\ 1\ 1]_{B2}$ Biot loading there is always a stable austenite branch for stresses where a stable martensite branch exists. The second difference is that for the $[1\ 1\ 1]_{B2}$ Biot loading at two lower temperatures there is a stable and continuous (tension and compression) martensite equilibrium path. However, as the temperature increases, the stable part of the martensite branch near zero stress disappears (see figure for $\theta=1.10$) while for even higher temperatures (see figures for $\theta=1.20$) there is a stable martensite branch in tension but not in compression.

The question that naturally arises here is whether pseudoelastic behavior is possible for the $[1\ 1\ 1]_{B2}$ Biot loading case. The affirmative answer to this question can be justified by looking at the corresponding energies in Fig. 12. Notice that for the lowest temperature $\theta=0.95$, the energy $\tilde{\mathcal{E}}$ is always lower for the martensite phase, while as the temperature increases, the austenite has a lower energy for the unstressed configuration (near $\lambda=1$) while for higher stresses the martensite branches have lower energy. When the equilibrium thermodynamics argument for phase transformation is used, i.e., when energy curves cross, a stress-induced transformation is possible according to the results depicted in Fig. 12, although the transformation stresses in compression, in particular, become large.

The disappearance of the compressive part of the martensite branch for the highest temperature $\theta=1.2$ seems odd at first glance. The explanation lies in the stretch ratio versus temperature graph for fixed stress levels (analogous to the results in Fig. 10) which are presented in Fig. 13. Due to the symmetry of the $[1\ 1\ 1]_{B2}$ Biot loading, all six variants of the stressed αIrV lattice are energetically equivalent, thus only one path is shown in Fig. 13. Notice that even for very high levels of compressive stresses ($\Sigma/C_{11}=-0.17$) there is no martensite branch for $\theta=1.2$. By contrast, a tensile martensite branch does exists at $\theta=1.2$ at a much lower stress ($\Sigma/C_{11}=0.05$). Hence, for this particular crystal and loading direction, it is found that the tension–compression asymmetry can lead to the absence of the compressive branch at sufficiently high temperatures.

3.5. Influence of loading device—uniaxial First Piola–Kirchhoff loading along the $[1\ 1\ 0]_{B2}$ direction

We now consider the application of Σ_0, force per reference area, along a fixed direction $\mathbf{N}$, where $\mathbf{N}$ is the reference configuration normal to the specimen's cross-section. Consequently, the specimen is subjected to a prescribed First Piola–Kirchhoff stress $\boldsymbol{\Pi}$, which corresponds to the applied pseudotraction $\mathbf{T}=\Sigma_0\mathbf{N}$, namely

$$\boldsymbol{\Pi}=\Sigma_0\mathbf{N}\mathbf{N},\quad \mathbf{T}=\mathbf{N}\cdot\boldsymbol{\Pi}, \tag{3.1}$$

and the conjugate strain measure is: $\mathbf{F}-\mathbf{I}$. The relationship between the Biot and First Piola–Kirchhoff stress is

$$\boldsymbol{\Pi}_B=\tfrac{1}{2}(\boldsymbol{\Pi}^T\cdot\mathbf{R}+\mathbf{R}^T\cdot\boldsymbol{\Pi}), \tag{3.2}$$

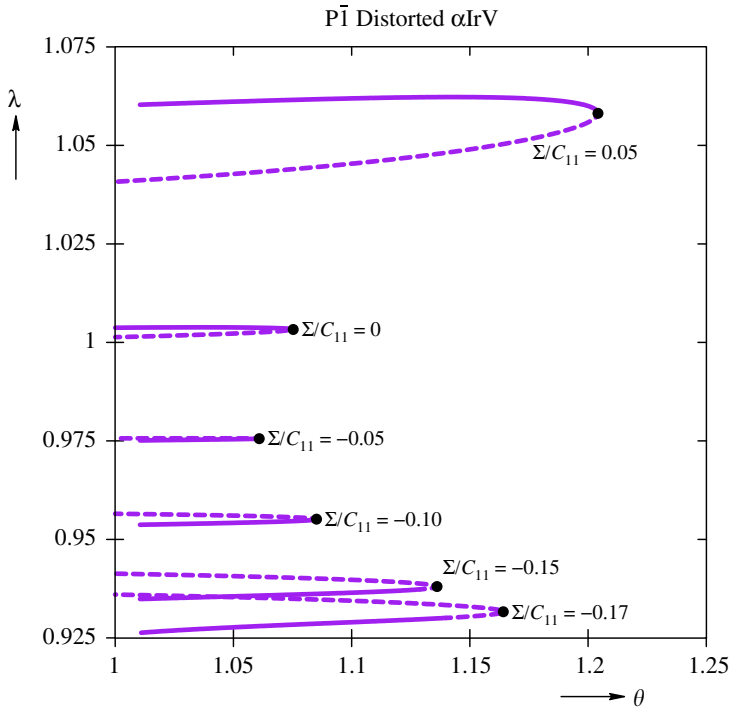

Fig. 13. Stretch ratio versus temperature at different stress levels for αIrV crystal structure for $[1\ 1\ 1]_{B2}$ Biot loading.

where **R** is the rotation tensor in the polar decomposition of **F**. The corresponding total potential energy per unit reference volume $\widehat{\mathcal{E}}$ can be written in terms of the internal energy per unit reference volume $\widehat{W}$ and the applied stress $\boldsymbol{\Pi}$ as

$$\widehat{\mathcal{E}} = \widehat{W} - \boldsymbol{\Pi}^T : (\mathbf{F}-\mathbf{I}) = \widehat{W} - \Sigma_0(\mathbf{N}\cdot\mathbf{F}\cdot\mathbf{N}-1), \tag{3.3}$$

where $\widehat{W}(\mathbf{C},\mathbf{S};\theta)$ is (for reasons of objectivity) a function of the Right Cauchy–Green tensor $\mathbf{C}\equiv\mathbf{F}^T\cdot\mathbf{F}$, internal shifts **S**, and temperature θ.

Of the nine dimensions of **F** only six are required to determine **C** and hence the crystal's stress state (but not its spatial orientation). The remaining three dimensions involve two rigid-body rotations about axes in the specimen cross-section $\mathbf{Y}_1$ and $\mathbf{Y}_2$ which are required to match the prescribed load orientation, and one arbitrary rotation about **N**. The presence of an arbitrary rotation about **N**, which follows from the invariance of $\widehat{\mathcal{E}}$ with respect to rigid-body rotations **Q** satisfying $\mathbf{N}\cdot\mathbf{Q}=\mathbf{N}$, can be eliminated by requiring

$$\mathbf{Y}_2\cdot\mathbf{F}\cdot\mathbf{Y}_1 = 0, \tag{3.4}$$

where $\{\mathbf{Y}_1, \mathbf{Y}_2, \mathbf{N}\}$ constitute an orthonormal triad with $\mathbf{Y}_1$, $\mathbf{Y}_2$ given directions within the plane initially perpendicular to **N**. The above requirement states that a material fiber initially along $\mathbf{Y}_1$ stays in the $(\mathbf{Y}_1, \mathbf{N})$ plane, i.e., $\mathbf{F}\cdot\mathbf{Y}_1$ is perpendicular to $\mathbf{Y}_2$.

The additional constraints to eliminate the remaining rigid-body degrees of freedom are found from the macroscopic equilibrium equations, i.e.,

$$\frac{\partial\widehat{\mathcal{E}}}{\partial\mathbf{F}} = \mathbf{F}\cdot\left(2\frac{\partial\widehat{W}}{\partial\mathbf{C}}\right) - \boldsymbol{\Pi}^T = \mathbf{0}, \tag{3.5}$$

which, with the help of Eq. (3.1) and after contracting both sides by $\mathbf{F}^T$, gives

$$\mathbf{F}\cdot\left(2\frac{\partial\widehat{W}}{\partial\mathbf{C}}\right)\cdot\mathbf{F}^T = \Sigma_0\mathbf{N}(\mathbf{N}\cdot\mathbf{F}^T). \tag{3.6}$$

The symmetry of the left-hand side of the above equation (which one can recognize as being the Kirchhoff stress) implies the symmetry of the right-hand side, i.e., **N** is parallel to $\mathbf{N}\cdot\mathbf{F}^T = \mathbf{F}\cdot\mathbf{N}$ and hence dictates, from the orthonormality of $\{\mathbf{Y}_1, \mathbf{Y}_2, \mathbf{N}\}$, that

$$\mathbf{Y}_1\cdot\mathbf{F}\cdot\mathbf{N} = \mathbf{Y}_2\cdot\mathbf{F}\cdot\mathbf{N} = 0. \tag{3.7}$$

The three independent constraints in Eqs. (3.4) and (3.7) can be used to regularize the equilibrium equations so that solutions to $\partial\widehat{\mathcal{E}}/\partial\mathbf{F}=\mathbf{0}$ provide isolated equilibrium paths stabilized with respect to rigid-body rotations that correspond to the physically motivated uniaxial loading path described here. A straightforward way to numerically implement the constrained

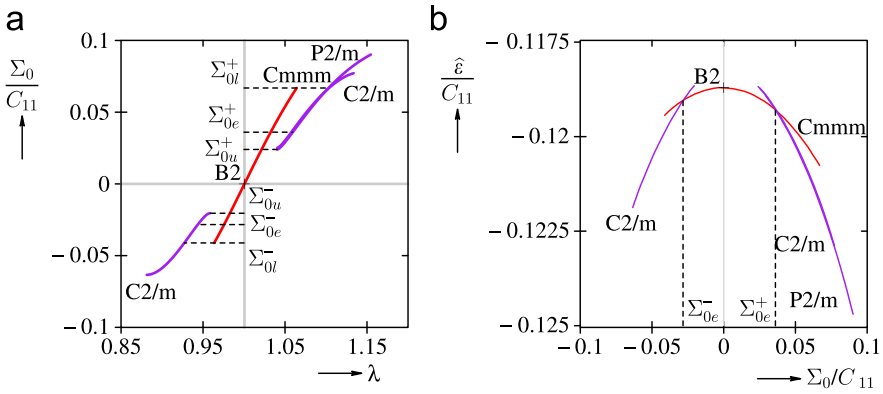

Fig. 14. Dimensionless stress versus conjugate stretch graphs for the martensite equilibrium paths in (a) and corresponding dimensionless energy density versus dimensionless stress shown in (b) for $[1\ 1\ 0]_{B2}$ uniaxial First Piola–Kirchhoff loading at $\theta = 1.2$.

equilibrium equations is by a penalty-type approach using the following expression for $\widehat{\mathcal{E}}$:

$$\widehat{\mathcal{E}} = \widehat{W} - \Sigma_0(\mathbf{N}\cdot\mathbf{F}\cdot\mathbf{N} - 1) + \frac{1}{2}(\mathbf{Y}_1\cdot\mathbf{F}\cdot\mathbf{Y}_2)^2 + \frac{1}{2\varepsilon}[(\mathbf{Y}_1\cdot\mathbf{F}\cdot\mathbf{N})^2 + (\mathbf{Y}_2\cdot\mathbf{F}\cdot\mathbf{N})^2], \tag{3.8}$$

where $1/\varepsilon$ is a penalty parameter. Notice, a penalty parameter is not required to eliminate the rigid-body constraint of Eq. (3.4) (see Jusuf, 2010), but one is necessary to impose the two constraints of Eq. (3.7). This stabilizes the equilibrium solutions subjected to compressive stresses with respect to rigid-body rotations. For this reason, the last two quadratic terms of Eq. (3.8) are associated with the small penalty parameter $0 < \varepsilon \ll 1$.

All results presented thus far correspond to equilibrium paths associated with an applied uniaxial Biot stress $\boldsymbol{\Pi}_B = \Sigma\mathbf{NN}$ (conjugate to the strain $\mathbf{U}-\mathbf{I}$). However, the above uniaxial First Piola–Kirchhoff stress formulation more faithfully represents realistic experimental conditions. Consequently it is worth recalculating, at least for the loading direction $[1\ 1\ 0]_{B2}$ and at a fixed temperature $\theta = 1.2$, the final equilibrium paths for a fixed-axis-loading, i.e., along paths for which the crystal is subjected to a uniaxial First Piola–Kirchhoff stress $\boldsymbol{\Pi} = \Sigma_0\mathbf{NN}$ (conjugate to the strain $\mathbf{F}-\mathbf{I}$). The equilibrium path calculations are this time based on the energy density given by Eq. (3.8) and the results are shown in Fig. 14.

Comparing Fig. 9 (uniaxial Biot loading) to Fig. 14 (uniaxial First Piola–Kirchhoff loading), both calculated for the same $[1\ 1\ 0]_{B2}$ direction and at the same temperature, one does not find any appreciable difference between them. Indeed the two corresponding sets of graphs (the stress versus stretch and energy versus stress) overlay each other to the naked eye. This observation justifies *a posteriori* the simplifying assumption of adopting a rotation-free equilibrium path for our calculations, since at least for our calculations, the influence of our *particular uniaxial* stress measure does not significantly affect the results.

4. Summary and conclusions

A modeling approach, based on temperature-dependent atomic potentials and path-following bifurcation techniques, has recently been introduced by the authors (Elliott et al., 2002, 2006a, b), to study the temperature-induced martensitic phase transformations in stress-free, perfect, equi-atomic binary B2 crystals. The same theoretical framework is used here to investigate the influence of stress on the thermomechanical instability responsible for stress-induced martensitic transformation of the same crystals.

In Elliott et al. (2006a) a bifurcation diagram of the material model's temperature-dependent, stress-free behavior was constructed. The high symmetry B2 cubic austenite structure's equilibrium path was found to transition from stable to unstable as the temperature decreased past a critical value, at which several bifurcated equilibrium paths emerged. Upon continuation, one of these paths becomes stable for lower temperatures, where the B2 phase is unstable at the same temperature. Furthermore, this path corresponded to the orthorhombic B19 crystal structure, which is a SMA martensite phase found in equi-atomic binary crystals.

In this work, a continuation of some preliminary investigations by Elliott (2007), the imposition of a uniaxial stress on the cubic B2 austenite crystal lowers the symmetry of the system, thus leading to a dramatic increase in the number of critical points found along the principal B2 path. This, in turn, results in a multitude of secondary paths bifurcating from the principal one with a large set of critical points found along each secondary path, and so on. Using continuation methods to follow all bifurcated equilibrium branches (the current investigation accounts for all branches up through the quartiary paths within a large window in temperature and stress space), hundreds of paths have been identified.

Consequently, one needs to determine which of these numerous equilibrium solutions are plausible reversible martensitic transformations. By investigating the stability of each branch, using the phonon and Cauchy–Born stability criteria discussed in Elliott et al. (2006b), one can eliminate most of the equilibrium paths as unstable. The final task is to determine which of the remaining stable equilibrium path segments, still relatively numerous, are possible reversible martensitic transformations. This selection relies on the *maximal Ericksen–Pitteri neighborhood* (max EPN) concept, a kinematic concept which selects those equilibrium solutions with lattice deformations which are *closest* to the reference austenite phase and thus likely to result in a reversible transformation.

It turns out that only one stable structure, a distorted αIrV crystal structure, is a martensitic transformation candidate within the max EPN of the austenite principal path in an appropriate stress window. Further investigation of the energy density of the corresponding configurations shows evidence of a phase transformation between the higher symmetry austenite and lower symmetry martensite paths and the existence of a hysteretic stress–strain loop under isothermal load–unload conditions. While the transformation strains calculated are reasonable compared to typical SMAs, the perfect crystal model over-predicts the critical stresses as well as the Clausious–Clapeyron slope when compared to experimental values measured from real polycrystalline samples. However, we believe that more sophisticated multiscale models are required to obtain quantitative agreement with this type of experimental data.

In conclusion, the present work is the first (to the best of our knowledge) that, using branch-following bifurcation techniques, has demonstrated the existence of both temperature-induced and stress-induced PTs—with the correct qualitative thermal and mechanical trends—in an atomistic perfect crystal model.

Acknowledgments

This work was supported by NSF grant—CMS 0409084 (Dr. Ken Chong, Program Director)—to the University of Michigan, by the NSF CAREER grant—CMMI-0746628 (Dr. Shih-Chi Liu, Program Director)—to the University of Minnesota, and by The University of Minnesota Supercomputing Institute.

Appendix A

A.1. Kinematics considerations

For the perfect bi-atomic lattices considered here, their stable, austenite stress-free configuration at the reference temperature is a B2 crystal structure. A four-lattice unit cell of the B2 structure—depicted in Fig. A1(a) in the (1 2 3) cubic symmetry axes system—is used (see Elliott et al., 2006a; Guthikonda and Elliott, 2008). However, a more convenient representation of the corresponding unit cell can be achieved in the system that is rotated by 45° about the 3-axis—the unit cell in the (*xyz*) system shown in Fig. A1(b). This Cauchy–Born kinematic description has 15 degrees of freedom, six for the uniform right stretch tensor **U** and nine for the three internal shift vectors **S**[1], **S**[2], **S**[3]. The reference lattice vectors for this description, oriented at 45° to the original cubic basis $\mathbf{G}_1$, $\mathbf{G}_2$, $\mathbf{G}_3$, are

$$\mathbf{G}_x = \mathbf{G}_1 + \mathbf{G}_2, \quad \mathbf{G}_y = -\mathbf{G}_1 + \mathbf{G}_2, \quad \mathbf{G}_z = \mathbf{G}_3. \tag{A.1}$$

The reference position vectors (see Eq. (2.1)) are given by

$$\mathbf{X}\begin{bmatrix} \ell \\ \alpha \end{bmatrix} = \mathbf{X}[\ell] + \mathbf{P}[\alpha],$$

$$\mathbf{X}[\ell] \equiv \ell^x \mathbf{G}_x + \ell^y \mathbf{G}_y + \ell^z \mathbf{G}_z,$$

$$\mathbf{P}[0] \equiv \mathbf{0}, \quad \mathbf{P}[1] \equiv \tfrac{1}{2}\mathbf{G}_x + \tfrac{1}{2}\mathbf{G}_z,$$

$$\mathbf{P}[2] \equiv \tfrac{1}{2}\mathbf{G}_x + \tfrac{1}{2}\mathbf{G}_y, \quad \mathbf{P}[3] \equiv \tfrac{1}{2}\mathbf{G}_y + \tfrac{1}{2}\mathbf{G}_z. \tag{A.2}$$

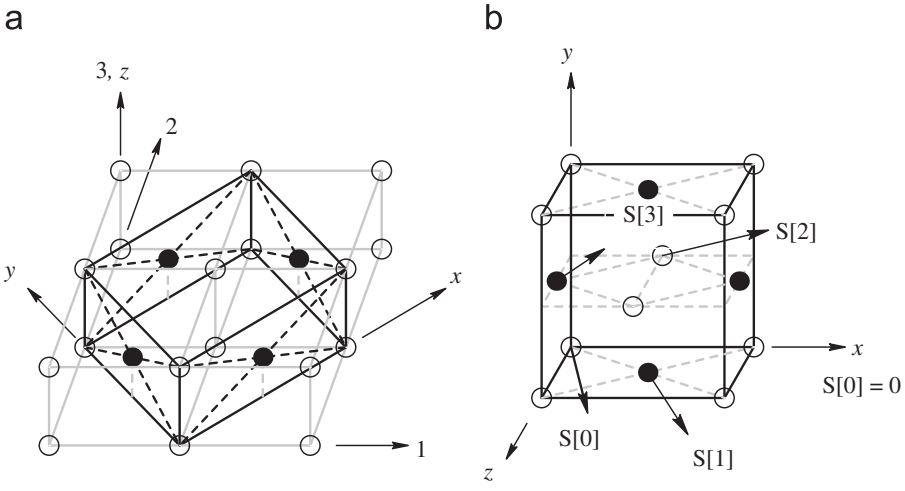

Fig. A1. Four-lattice model: (a) 123 cubic coordinate system, (b) *xyz* tetragonal coordinate system.

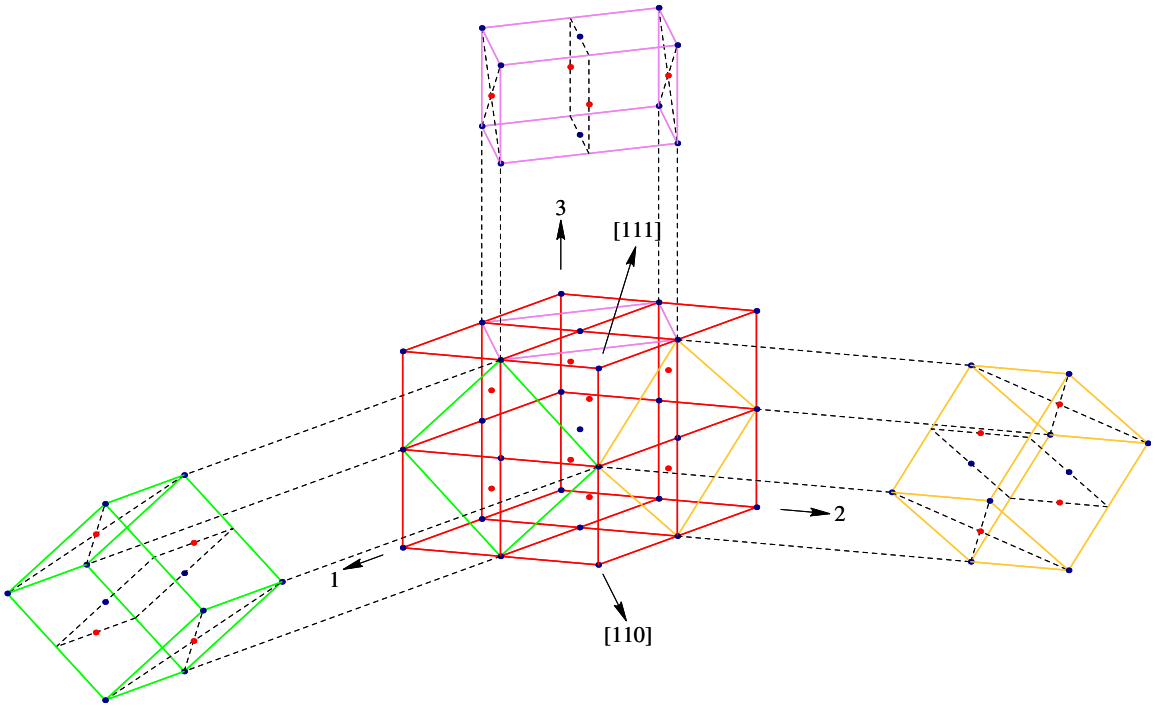

Fig. A2. A $2 \times 2 \times 2$ cubic cell of the B2 crystal and the associated three distinct four-lattice representations contained within it.

Unfortunately, this set of kinematics is not able to fully express the cubic symmetry of the reference configuration. In particular, the 120° and 240° rotations about the $[1\,1\,1]_{(123)}$ axis, map the four-lattice unit cell into two distinct (inequivalent) four-lattice representations of the B2 structure. This is illustrated in Fig. A2. Because each of the three four-lattice representations are inequivalent they lead to different lattice configurations under stress. For this reason, the uniaxial stress state was applied separately to each of the three inequivalent four-lattice representations.

A.2. Potential choice

The general methodology described above is applicable to any type of atomic potential. Here, we aim to study the thermoelastic behavior of the alloy without explicitly simulating the kinetic energy of the atoms. Therefore, a set of "effective" interaction potentials (EIPs) are postulated to exist at each temperature. The intent of these phenomenological EIPs is to capture the dominant characteristics of the material's free energy, including both potential energy and entropic effects. Accordingly, Eq. (2.6) should be understood to provide the essential structure of the alloy's Helmholtz free energy (as a function of configuration and temperature). Additional entropic-based terms may be required to ensure that the material model satisfies all standard thermodynamic requirements (as shown recently by Guthikonda and Elliott, 2008, 2009, in press), but these effects are not expected to significantly alter the energy landscape defined by Eq. (2.6).

For simplicity, temperature-dependent pair potentials are used here. Despite the known shortcomings of pair potentials, they have been used successfully in modeling the behavior of lattice-level instabilities related to phase transformations in perfect crystals. More specifically, a set of temperature-dependent Morse pair potentials is adopted to model typical bi-atomic SMAs such as NiTi and AuCd. The current atomic interaction model is a slightly modified version of that used by Elliott et al. (2006a). The general form of the potential is

$$\phi(r;\theta) = A\left\{\exp\left[-2B\left(\frac{r}{\widehat{r}(\theta)}-1\right)\right]-2\exp\left[-B\left(\frac{r}{\widehat{r}(\theta)}-1\right)\right]\right\},$$

$$\widehat{r}(\theta) = (r_0 + r_\theta(\theta-1))(t_0 + t_\theta(\theta-1)), \tag{A.3}$$

where A, B, r_0, r_θ, t_0, and t_θ are bond parameters, and $\theta \equiv T/T_{\text{ref}}$ is the normalized temperature. The reference temperature is taken to be T_{ref}=300 K. In this work the pair-equilibrium separation $\widehat{r}(\theta)$ is taken to be a quadratic function of the normalized temperature, instead of the linear function used previously. This modification provides the material model with enough flexibility to fit the thermal expansion coefficient of a given material. For the binary material considered here a set of three potentials is required, ϕ_{00}, ϕ_{11}, and ϕ_{01}, corresponding to pair-interactions between two 0 atoms, two 1 atoms, and interactions between a 0 atom and a 1 atom, respectively. The particular values of the six parameters for each of these potentials is given in Table A1. These parameters were chosen in a manner similar to that described in Elliott et al. (2006a), and the thermal expansion coefficient of NiTi austenite (B2 cubic structure) at the reference temperature ($\theta = 1$) was matched by the choice of t_0 and t_θ for the three bonds.

Table A1
Pair potential parameters used for the three temperature-dependent atomic potentials.

Bond	A	B	r_0	r_θ	t_0	t_θ
0 0	0.0135279	4.0	1.0	0.0	1.0	−0.1461572
1 1	0.0135279	7.0	1.1492407809	0.2759143763	1.0	−0.1461572
0 1	0.0135279	5.5	1.0708087476	0.1379571881	1.0	−0.1461572

The work of Guthikonda and Elliott (2008) considers the sensitivity of the Morse potential model for B2-type alloys. There it is found that the qualitative features of the energy landscape are highly robust to parameter variations. Consequently, the stable crystal structures discovered in this work remain stable over a remarkably wide range of the Morse potential's constants.

References

Allgower, E.L., Georg, K., 2003. Introduction to numerical continuation methods. Classics in Applied Mathematics, vol. 45. SIAM.

Bhattacharya, K., 2003. In: Microstructure of Martensite: Why it Forms and How it Gives Rise to the Shape-memory Effect. Oxford Series on Materials Modelling first ed. Oxford University Press.

Bhattacharya, K., Conti, S., Zanzotto, G., Zimmer, J., 2004. Crystal symmetry and the reversibility of martensitic transformations. Nature 428 (6978), 55–59.

Conti, S., Zanzotto, G., 2004. A variational model for reconstructive phase transformations in crystals, and their relation to dislocations and plasticity. Archive for Rational Mechanics and Analysis 173, 69–88.

Ding, X., Suzuki, T., Ren, X., Sun, J., Otsuka, K., 2006. Precursors to stress-induced martensitic transformations and associated superelasticity: molecular dynamics simulations and an analytical theory. Physical Review B—Condensed Matter 74 1041111-1–1041111-10.

Elliott, R.S., 2007. Multiscale bifurcation and stability of multilattices. Journal of Computer-Aided Materials Design 14 (Suppl. 1), 143–157.

Elliott, R.S., 2010. Branch-following and bifurcation with symmetry package (BFBSymPac). Available by request from the author, elliott@aem.umn.edu.

Elliott, R.S., Karls, D.S., submitted. Entropic stabilization of austenite in shape memory alloys. Journal of the Mechanics and Physics of Solids.

Elliott, R.S., Shaw, J.A., Triantafyllidis, N., 2002. Stability of thermally-induced martensitic transformations in bi-atomic crystals. Journal of the Mechanics and Physics of Solids 50 (11), 2463–2493.

Elliott, R.S., Shaw, J.A., Triantafyllidis, N., 2006a. Stability of crystalline solids—II: application to temperature-induced martensitic phase transformations in bi-atomic crystals. Journal of the Mechanics and Physics of Solids 54 (1), 193–232.

Elliott, R.S., Triantafyllidis, N., Shaw, J.A., 2006b. Stability of crystalline solids—I: continuum and atomic-lattice considerations. Journal of the Mechanics and Physics of Solids 54 (1), 161–192.

Entel, P., Kadau, K., Meyer, R., Herper, H.C., Schroter, M., Hoffmann, E., 1999. Large-scale molecular-dynamics simulations of martensitic nucleation and shape-memory effects in transition metal alloys. Phase Transitions 65, 79–108.

Entel, P., Meyer, R., Kadau, K., 2000. Molecular dynamics simulations of martensitic transitions. Philosophical Magazine B—Physics of Condensed Matter Statistical Mechanics Electronic Optical and Magnetic Properties 80 (2), 183–194.

Ericksen, J.L., 1980. Some phase transitions in crystals. Archive for Rational Mechanics and Analysis 73 (2), 99–124.

Ericksen, J.L., 1992. Bifurcation and martensitic transformations in Bravais lattices. Journal of Elasticity 28, 55–78.

Gall, K., Sehitoglu, H., Chumlyokov, Y.I., Kireeva, I.V., 1999. Tension–compression asymmetry of the stress–strain response in aged single crystal and polycrystalline NiTi. Acta Metallurgica 47 (4), 1203–1217.

Grujicic, M., Dang, P., 1995. Computer simulation of martensitic transformation in Fe–Ni face-centered cubic alloys. Materials Science & Engineering A 201, 194–204.

Guthikonda, V.S., Elliott, R.S., 2008. Stability and elastic properties of the stress-free B2 (CsCl-type) crystal for the Morse pair potential model. Journal of Elasticity 92 (2), 151–186.

Guthikonda, V.S., Elliott, R.S., 2009. An effective interaction potential model for the shape memory alloy AuCd. Continuum Mechanics and Thermodynamics 21 (4), 269–295.

Guthikonda, V.S., Elliott, R.S., in press. Erratum to: an effective interaction potential model for the shape memory alloy AuCd. Continuum Mechanics and Thermodynamics., doi:10.1007/s00161-009-0109-1.

Healey, T.J., 1988. A group-theoretic approach to computational bifurcation problems with symmetry. Computer Methods in Applied Mechanics and Engineering 67, 257–295.

Healey, T.J., Miller, U., 2007. Two-phase equilibria in the anti-plane shear of an elastic solid with interfacial effects via global bifurcation. Proceedings of the Royal Society of London Series A—Mathematical and Physical Sciences 463, 1117–1134.

Huang, X., Ackland, G.J., Rabe, K.M., 2003a. Crystal structures and shape-memory behaviour of NiTi. Nature Materials 2 (5), 307–311.

Huang, X., Bungarao, C., Godlevsky, V., Rabe, K.M., 2002. Lattice instabilities of cubic NiTi from first principles. Physical Review B—Condensed Matter 65 (1), 1–5.

Huang, X., Rabe, K.M., Ackland, G.J., 2003b. Crystal structures and shape-memory behavior of NiTi. Nature Materials 2 (5), 307–311.

Ishida, H., Hiwatari, Y., 2007. MD simulation of martensitc transformations in TiNi alloys with MEAM. Molecular Simulation 33, 459–461.

Jusuf, V., 2010. Algorithms for branch-following and critical point identification in the presence of symmetry. Master's Thesis, Department of Aerospace Engineering and Mechanics, The University of Minnesota, Minneapolis, MN, USA.

Meyer, R., Entel, P., 1998. Martensite–austenite transition and phonon dispersion curves of $Fe_{1-x}Ni_x$ studied by molecular-dynamics simulations. Physical Review B 57 (9), 5140–5147.

Milstein, F., Hill, R., Huang, K., 1980. Theory of the response of cubic crystals to [1 1 1] loading. Physical Review B—Condensed Matter 21 (10), 4282–4291.

Milstein, F., Marschall, J., Fang, H.E., 1995. Theoretical bcc $<=>$ fcc transitions in metals via bifurcations under uniaxial load. Physical Review Letters 74 (15), 2977–2980.

Otsuka, K., Wayman, C.M., 1998. Shape Memory Materials. Cambridge University Press.

Ozgen, S., Adiguzel, O., 2003. Molecular dynamics simulations of diffusionless phase transformation in quenched NiAl alloy model. Journal of Physics and Chemistry of Solids 64 (3), 459–464.

Parlinski, K., Parlinska, M., Gotthardt, R., 2003. Phonons in austenite and martensite NiTi crystals. Journal De Physique IV 112, 635–638.

Parlinski, K., Parlinska-Wojtan, M., 2002. Lattice dynamics of NiTi austenite, martensite, and R phase. Physical Review B 67 (064307), 1–8.

Pitteri, M., 1984. Reconciliation of local and global symmetries of crystals. Journal of Elasticity 14, 175–190.

Pitteri, M., 2003a. Full kinematics of $\beta-$quartz in the view of its weak phase transformations. In: Notices of Universities. South of Russia. Natural sciences., 2nd special issue: Nonlinear problems of Continuum Mechanics, Dedicated to 60th birthday of Professor L.M. Zubov, pp. 3145–3172.

Pitteri, M., 2003b. On certain weak phase transformations in multilattices. Journal of Elasticity 72, 241–261.

Pitteri, M., Zanzotto, G., 2002. Continuum Models for Phase Transitions and Twinning in Crystals. In: Applied Mathematics, vol. 19. Chapman & Hall.
Riks, E., 1979. Incremental approach to the solution of snapping and buckling problems. International Journal of Solids and Structures 15 (7), 529–551.
Rubini, S., Ballone, P., 1995. Martensitic transformations and phonon localization in Ni–Al alloys by atomistic simulations. Meccanica 30, 439–448.
Shao, Y., Clapp, P.C., Rifkin, J.A., 1996. Molecular dynamics simulation of martensitic transformations in NiAl. Metallurgical and Materials Transactions A 27A, 1477–1489.
Shaw, J.A., Kyriakides, S., 1995. Thermomechanical aspects of NiTi. Journal of the Mechanics and Physics of Solids 43 (8), 1243–1281.
Stokes, H.T., Hatch, D.M., Dong, J., Lewis, J.P., 2004. Mechanisms for the reconstructive phase transition between the B1 and B2 structure types in NaCl and PbS. Physical Review B—Condensed Matter 69 (17) 174111-1–174111-5.
Thompson, J.M.T., Hunt, G.W., 1984. Elastic Instability Phenomena, first ed. John Wiley & Sons.
Thompson, J.M.T., Shorrock, P.A., 1975. Bifurcational instability of an atomic lattice. Journal of the Mechanics and Physics of Solids 23, 21–37.
Triantafyllidis, N., Peek, R., 1992. On stability and the worst imperfection shape in solids with nearly simultaneous eigenmodes. International Journal of Solids and Structures 29 (18), 2281–2299.
Wang, J., Wang, Y., Schaublin, R., Abromeit, C., Gotthardt, R., 2006. The effect of point defects on the martensitic phase transformation. Material Science and Engineering A—Structural Material Properties Microstructure and Processing 438, 102–108.
Wohlever, J., Healey, T.J., 1995. A group theoretic approach to the global bifurcation analysis of an axially compressed cylindrical shell. Computer Methods in Applied Mechanics and Engineering 122, 315–349.
Ye, Y.Y., Chan, C.T., Ho, K.M., 1997. Structural and electronic properties of the martensitic alloys TiNi, TiPd and TiPt. Physical Review B 56 (7), 3678–3689.